

1 Reply to comments

2

3 Dear editor,

4

5 Thanks for your comments. In the following, we have addressed the comment, with the
6 original review text underlined in italics and red.

7

8 *Perhaps the most important reviewer's point that I do not feel has been addressed here is*
9 *made clear by the reviewers comment 'Line 492: Yes, the parameters are somewhere in*
10 *the range of the right magnitude, but not more. It would be great if this study would help*
11 *to represent $^{231}\text{Pa}/^{230}\text{Th}$ in a realistic model, not only somewhere in the range of a*
12 *factor of 25.'* *The point being made is that there is observational data which can help*
13 *constrain the parameters. The review has clearly asked in a number of places for an*
14 *experiment to be done with parameters chosen to reflect this understanding. Please can*
15 *you either undertake this experiment, or justify robustly why you do not feel that this is*
16 *useful?*

17

18 *Your argument against this is (1) it is not feasible to undertake a large ensemble of*
19 *sensitivity experiments, and (2) the model does an adequate job of capturing the major*
20 *features as it is. However:*

21

22 *(1) Here the reviewer is not asking for a large sensitivity analysis, simply a single run to*
23 *be done with more realistic parameters, i.e. parameters derived from observations. I*
24 *would imagine that this is not too resource intensive?*

25

26 *(2) If the model is capturing the observed behaviour with unrealistic parameters, either*
27 *the parameters are not important, or there is something wrong.*

28

29 *Please can you either perform this simulation and present the results, or explain why this*
30 *is not a sensible approach?*

31

32 First of all, to answer your question 2 “*If the model is capturing the observed behavior*
33 *with unrealistic parameters....*”, the parameters used in our control experiment is not
34 unrealistic. It is suggested by observations (Chase et al., 2002). In the two sensitivity
35 experiments, we increase and decrease the parameters by a factor of 5 (line 217), not a
36 factor of 25 (in the reviewer’s comment). Compared with two sensitivity experiments, the
37 control experiment is better simulating Pa and Th (discussed in section 4.2). Therefore,
38 we state that “the partition coefficient in CTRL is of the right order of magnitude”. Using
39 the parameters suggested by observation (Chase et al., 2002), our model is able to capture
40 the major features of Pa and Th.

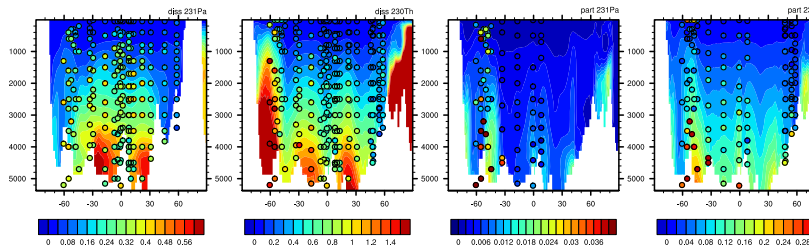
41

42 We do have an experiment with parameters increased by a factor of 1.5 (Exp3). The
43 results of Exp3 is similar to CTRL. The water column dissolved Pa and Th (Fig. R1) is
44 slightly smaller than CTRL (Fig. S3) because of the increased partition coefficient (line
45 330). The interbasin gradient of sediment $^{231}\text{Pa}/^{230}\text{Th}$ in Exp3 (Fig. R3) is also slightly
46 smaller than CTRL (Fig. 4) (line 348). The performance of CTRL is better than Exp3 in

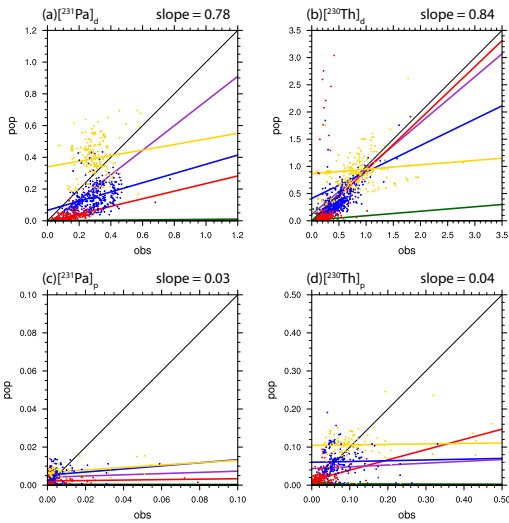
47 that the regression coefficient of sediment $^{231}\text{Pa}/^{230}\text{Th}$ is 0.2 in CTRL and 0.11 in Exp3
48 globally; 0.86 in CTRL and 0.77 in Exp3 in the Atlantic; 0.16 in CTRL and 0.02 in Exp3
49 in the Pacific; 0.18 in CTRL and 0.11 in Exp3 in the Southern Ocean. Overall, the
50 difference between Exp3 and CTRL is similar to the difference between Exp2 (increase
51 parameters by a factor of 5) and CTRL, but with much smaller magnitude. Therefore, we
52 don't feel it is necessary to show the results of Exp3 in the text.

53
54 In Exp3, we only change the magnitude of the partition coefficients and keep the relative
55 fractionation factor by different particles the same. However, fractionation factor
56 suggested by different studies also varies (Table A1 from Rempfer et al., 2017).
57 Therefore, when tuning parameters in future studies, both magnitude of partition
58 coefficients and the fractionation factor by different particles should vary systematically
59 to test which combination yields the best results (this is also discussed in our previous
60 reply to comments). But at current stage, this kind of experiments is beyond our
61 resources.

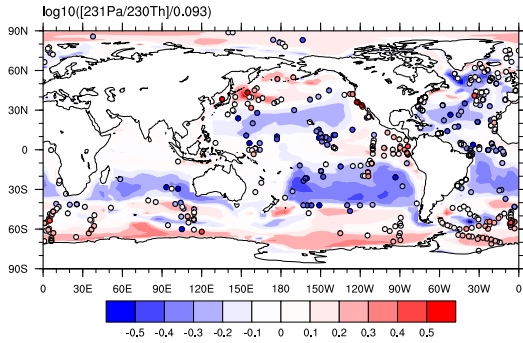
62
63



64
65 Figure R1. Atlantic zonal mean dissolved and particulate ^{231}Pa and ^{230}Th in Exp3.
66



67
 68 Figure R2. Scatter plot of global dissolved and particulate ^{231}Pa and ^{230}Th between
 69 observation and model results in Exp3 (unit: dpm/m³). (a) dissolved ^{231}Pa ; (b) particulate
 70 ^{231}Pa ; (c) dissolved ^{230}Th ; (d) particulate ^{230}Th . Lines and colors are the same in Figure 5.
 71



72
 73 Figure R3. Sediment $^{231}\text{Pa}/^{230}\text{Th}$ activity ratio in Exp3. Observations are attached as filled
 74 cycles using the same color map.
 75

76 Reference:
 77 Chase, Z., Anderson, R. F., Fleisher, M. Q., & Kubik, P. W. (2002). The influence of
 78 particle composition and particle flux on scavenging of Th, Pa and Be in the ocean.
 79 *Earth and Planetary Science Letters*, 204(1–2), 215–229.
 80 [https://doi.org/10.1016/S0012-821X\(02\)00984-6](https://doi.org/10.1016/S0012-821X(02)00984-6)
 81 Rempfer, J., Stocker, T. F., Joos, F., Lippold, J., & Jaccard, S. L. (2017). New insights

82 into cycling of ^{231}Pa and ^{230}Th in the Atlantic Ocean. *Earth and Planetary*
83 *Science Letters*, 468, 27–37. <https://doi.org/10.1016/j.epsl.2017.03.027>
84

85 **^{231}Pa and ^{230}Th in the ocean model of the Community Earth System Model**
86 **(CESM1.3)**
87 Sifan Gu¹, Zhengyu Liu²

88

89 ¹Department of Atmospheric and Oceanic Sciences and Center for Climate Research,
90 University of Wisconsin-Madison, Madison, WI, USA

91 ²Atmospheric Science Program, Department of Geography, Ohio State University,
92 Columbus, OH, USA

93

94 Correspondence to: Sifan Gu (sgu28@wisc.edu)

95

96 Abstract

97 Sediment $^{231}\text{Pa}/^{230}\text{Th}$ activity ratio is emerging as an important proxy for
98 deep ocean circulation in the past. In order to allow for a direct model-data
99 comparison and to improve our understanding of sediment $^{231}\text{Pa}/^{230}\text{Th}$ activity
100 ratio, we implement ^{231}Pa and ^{230}Th in the ocean component of the Community
101 Earth System Model (CESM). In addition to the fully coupled implementation of the
102 scavenging behavior of ^{231}Pa and ^{230}Th with the active marine ecosystem module (p-
103 coupled), another form of ^{231}Pa and ^{230}Th have also been implemented with
104 prescribed particle flux fields of the present climate (p-fixed). The comparison of the
105 two forms of ^{231}Pa and ^{230}Th helps to isolate the influence of the particle fluxes from
106 that of ocean circulation. Under present day climate forcing, our model is able to
107 simulate water column ^{231}Pa and ^{230}Th activity and sediment $^{231}\text{Pa}/^{230}\text{Th}$ activity
108 ratio in good agreement with available observations. In addition, in response to
109 freshwater forcing, the p-coupled and p-fixed sediment $^{231}\text{Pa}/^{230}\text{Th}$ activity ratios
110 behave similarly over large areas of low productivity on long timescale, but can
111 differ substantially in some regions of high productivity and on short timescale,
112 indicating the importance of biological productivity in addition to ocean transport.
113 Therefore, our model provides a potentially powerful tool to help the interpretation
114 of sediment $^{231}\text{Pa}/^{230}\text{Th}$ reconstructions and to improve our understanding of past
115 ocean circulation and climate changes.

116 **1. Introduction**

117 Sediment $^{231}\text{Pa}/^{230}\text{Th}$ activity ratio has been one major proxy for ocean
118 circulation in the past (e.g. Yu et al. 1996; McManus et al. 2004; Gherardi et al.
119 2009). ^{231}Pa (32.5 ka half-life) and ^{230}Th (75.2 ka half-life) are produced at a
120 constant rate approximately uniformly in the ocean by the α decay of ^{235}U and ^{234}U ,
121 respectively, with a production activity ratio of 0.093 (Henderson and Anderson,
122 2003). Water column ^{231}Pa and ^{230}Th are subject to particle scavenging and
123 transport to sediments (Bacon and Anderson, 1982; Nozaki et al., 1987). Different
124 scavenging efficiency results in different ocean residence time: ^{231}Pa has a residence
125 time of approximately 111 years and ^{230}Th has a residence time of approximately 26
126 years (Yu et al., 1996). Longer residence time of ^{231}Pa than ^{230}Th makes ^{231}Pa more
127 subject to ocean transport and therefore in the modern ocean about 45% of ^{231}Pa
128 produced in the Atlantic is transported to the Southern Ocean (Yu et al., 1996),
129 resulting a lower than 0.093 sediment $^{231}\text{Pa}/^{230}\text{Th}$ activity ratio in the North Atlantic
130 and higher than 0.093 sediment $^{231}\text{Pa}/^{230}\text{Th}$ activity ratio in the Southern Ocean.

131 The application of the principle above to interpret sediment $^{231}\text{Pa}/^{230}\text{Th}$ as
132 the strength of Atlantic meridional overturning circulation (AMOC), however, can be
133 complicated by other factors, leading to uncertainties in using $^{231}\text{Pa}/^{230}\text{Th}$ as a proxy
134 for past circulation (Keigwin and Boyle, 2008; Lippold et al., 2009; Scholten et al.,
135 2008). In addition to the ocean transport, sediment $^{231}\text{Pa}/^{230}\text{Th}$ is also influenced by
136 particle flux and composition (Chase et al., 2002; Geibert and Usbeck, 2004;
137 Scholten et al., 2008; Siddall et al., 2007; Walter et al., 1997). The region of a higher
138 particle flux tends to have a higher $^{231}\text{Pa}/^{230}\text{Th}$ (Kumar et al., 1993; Yong Lao et al.,
139 1992), which is referred to as the “particle flux effect” (Siddall et al., 2005). Regional
140 high particle flux in the water column will favor the removal of isotopes into the
141 sediment, which leads to more isotopes transported into this region due to the
142 down-gradient diffusive flux and subsequently more removal of isotopes into the
143 sediment. Since ^{231}Pa has a longer residence time, this effect is more prominent on
144 ^{231}Pa than on ^{230}Th and therefore sediment $^{231}\text{Pa}/^{230}\text{Th}$ will be higher in high
145 productivity regions. Also, opal is able to scavenge ^{231}Pa much more effectively than
146 ^{230}Th , leading to higher $^{231}\text{Pa}/^{230}\text{Th}$ in high opal flux regions such as the Southern

147 Ocean (Chase et al., 2002). Moreover, sediment $^{231}\text{Pa}/^{230}\text{Th}$ is suggested to record
148 circulation change only within 1,000 m above the sediment, instead of the whole
149 water column, complicating the interpretation of sediment $^{231}\text{Pa}/^{230}\text{Th}$
150 reconstructions (Thomas et al., 2006). For example, sediment $^{231}\text{Pa}/^{230}\text{Th}$
151 approaching 0.093 during Heinrich Stadial event 1(HS1) from the subtropical North
152 Atlantic is interpreted as the collapse of AMOC (McManus et al., 2004). If sediment
153 $^{231}\text{Pa}/^{230}\text{Th}$ only records deepest water mass, it is possible that during HS1, AMOC
154 shoals, as opposed to a fully collapse, yet an increase of deep water imported from
155 the Southern Ocean featuring high $^{231}\text{Pa}/^{230}\text{Th}$ can increase the sediment
156 $^{231}\text{Pa}/^{230}\text{Th}$ approaching the production ratio (0.093) (Thomas et al., 2006).
157 Therefore, it is important to incorporate ^{231}Pa and ^{230}Th into climate models for a
158 direct model-data comparison and to promote a thorough understanding of
159 sediment $^{231}\text{Pa}/^{230}\text{Th}$ as well as past ocean circulation.

160 ^{231}Pa and ^{230}Th have been simulated in previous modeling studies (Dutay et
161 al., 2009; Luo et al., 2010; Marchal et al., 2000; Rempfer et al., 2017; Siddall et al.,
162 2005). Marchal et al., (2000) simulates ^{231}Pa and ^{230}Th in a zonally averaged
163 circulation model, using the reversible scavenging model of Bacon and Anderson,
164 (1982). One step further, Siddall et al. (2005) extends Marchal et al., (2000) by
165 including particle dissolution with prescribed particle export production in a 3-D
166 circulation model. Rempfer et al., (2017) further couples ^{231}Pa and ^{230}Th with active
167 biogeochemical model and includes boundary scavenging and sediment
168 resuspensions to improve model performance in simulating water column ^{231}Pa and
169 ^{230}Th activity. Here we follow previous studies to implement ^{231}Pa and ^{230}Th into the
170 Community Earth System Model (CESM). Our standard ^{231}Pa and ^{230}Th are coupled
171 with active marine ecosystem model (“p-coupled”) and therefore is influenced by
172 both ocean circulation change and particle flux change. To help to understand the
173 influence of the particle flux, we have also implemented an auxiliary version of
174 ^{231}Pa and ^{230}Th (“p-fixed”) for which the particle fluxes are fixed at prescribed
175 values. Therefore, p-fixed $^{231}\text{Pa}/^{230}\text{Th}$ is only influenced by ocean circulation change.
176 By comparing the p-fixed $^{231}\text{Pa}/^{230}\text{Th}$ with the p-coupled $^{231}\text{Pa}/^{230}\text{Th}$, we will be
177 able to separate the effect of circulation change from particle flux change. In

178 addition, the p-fixed ^{231}Pa and ^{230}Th can be run without the marine ecosystem
179 module, reducing computational cost by a factor of 3 in the ocean-alone model
180 simulation, making it a computationally efficient tracer for sensitivity studies.

181 This paper describes the details of ^{231}Pa and ^{230}Th in CESM and serves as a
182 reference for future studies using this tracer module. In section 2, we describe the
183 model and the implementation of ^{231}Pa and ^{230}Th . In sections 3, we describe the
184 experimental design. We will finally compare simulated ^{231}Pa and ^{230}Th fields with
185 observations, show model sensitivities on model parameter and also sediment
186 $^{231}\text{Pa}/^{230}\text{Th}$ ratio response to freshwater forcing in Section 4.

187

188 **2. Model Description**

189 2.1 Physical Ocean Model

190 We implement ^{231}Pa and ^{230}Th in the ocean model (Parallel Ocean Program
191 version 2, POP2) (Danabasoglu et al., 2012) of CESM (Hurrell et al., 2013). CESM is a
192 state-of-the-art coupled climate model and studies describing model components
193 and analyzing results can be found in a special collection in Journal of Climate
194 (<http://journals.ametsoc.org/topic/ccsm4-cesm1>). We run the ocean-alone model,
195 which is coupled to data atmosphere, land, ice and river runoff under the normal
196 year forcing of CORE-II data (Large and Yeager, 2008), using the low-resolution
197 version of POP2 with a nominal 3° horizontal resolution and 60 vertical layers.

198

199 2.2 Biogeochemical component (BGC)

200 CESM has incorporated a marine ecosystem module that simulates biological
201 variables (Moore et al., 2013). The marine ecosystem module has been validated
202 against present day observations extensively (e.g. Doney et al., 2009; Long et al.,
203 2013; Moore et al., 2002, 2004; Moore and Braucher, 2008). The implementation of
204 ^{231}Pa and ^{230}Th requires particle fields: CaCO_3 , opal and particulate organic carbon
205 (POC). These particle fields can be obtained through the ecosystem driver from the
206 ecosystem module (Jahn et al., 2015). The ecosystem module simulates the particle
207 fluxes in reasonable agreement with the present-day observations. The pattern and
208 magnitude of the annual mean particle fluxes (CaCO_3 , opal, POC) leaving the

209 euphotic zone at 105m are similar to the satellite observations (Fig. 7.2.5 and 9.2.2
 210 in Sarmiento and Gruber 2006) (Fig. 1 a~c): particle fluxes are higher in the high
 211 productivity regions such as high latitudes and equatorial Pacific; opal flux is high in
 212 the Southern Ocean. The remineralization scheme of particle is based on the ballast
 213 model of Armstrong et al., (2002). Detailed parameterizations for particle
 214 remineralization are documented in Moore et al., (2004) with temperature
 215 dependent remineralization length scales for POC and opal. We do not consider dust
 216 because it is suggested to be unimportant for ^{231}Pa and ^{230}Th fractionation (Chase et
 217 al., 2002; Siddall et al., 2005).

218

219 2.3 ^{231}Pa and ^{230}Th implementation

220 ^{231}Pa and ^{230}Th are produced from the α decay of ^{235}U and ^{234}U uniformly
 221 everywhere at constant rate β^i ($\beta^{\text{Pa}} = 2.33 \cdot 10^{-3} \text{ dpm m}^{-3} \text{ yr}^{-1}$, $\beta^{\text{Th}} = 2.52 \cdot 10^{-2} \text{ dpm m}^{-3}$
 222 yr^{-1}). ^{231}Pa and ^{230}Th are also subjective to radioactive decay with the decay
 223 constant of λ^i ($\lambda^{\text{Pa}} = 2.13 \cdot 10^{-5} \text{ yr}^{-1}$, $\lambda^{\text{Th}} = 9.22 \cdot 10^{-6} \text{ yr}^{-1}$).

224 Another important process contributes to ^{231}Pa and ^{230}Th activity is the
 225 reversible scavenging by sinking particles (Bacon and Anderson, 1982), which
 226 describes the adsorption of isotopes onto sinking particles and desorption after the
 227 dissolution of particles. This process transports ^{231}Pa and ^{230}Th downward and
 228 leads to a general increase of ^{231}Pa and ^{230}Th activity with depth. The reversible
 229 scavenging considers total isotope activity (A_t^i) as two categories (Eq. (1)):
 230 dissolved isotopes (A_d^i) and particulate isotopes (A_p^i) (superscript i refers to ^{231}Pa
 231 and ^{230}Th) and A_p^i is the sum of the isotopes associated with different particle types
 232 ($A_{j,p}^i$) (subscript j refers to different particle types: CaCO_3 , opal and POC):

$$233 \quad A_t^i = A_d^i + A_p^i = A_d^i + \sum_j A_{j,p}^i \quad (1)$$

234

235 Dissolved and particulate isotopes are assumed to be in equilibrium, which is a
 236 reasonable assumption in the open ocean (Bacon and Anderson, 1982; Henderson et

237 al., 1999; Moore and Hunter, 1985). The ratio between the particulate isotope
238 activity and the dissolved isotope activity is set by a partition coefficient, K (Eq. (2)):

$$239 \quad K_j^i = \frac{A_{j,p}^i}{A_d^i \cdot R_j} \quad (2)$$

240
241 , where R_j is the ratio of particle concentration (C_j) to the density of seawater
242 (1024.5 kg m^{-3}). Subscript j refers to different particle types (CaCO_3 , opal and POC).
243 Values of partition coefficient K used in our control simulation follows Chase et al.,
244 2002 and Siddall et al., 2005 (Table 2).

245 Particulate isotopes (A_p^i) will be transported by sinking particles, which is
246 described by $w_s \frac{\partial A_p^i}{\partial z}$ (Eq. (3)), where w_s is the sinking velocity. We don't
247 differentiate between slow sinking small particles and rapid sinking large particles
248 as in Dutay et al., (2009) and consider all particles as slowly sinking small particles
249 with sinking velocity of $w_s = 1000 \text{ m yr}^{-1}$ (Arsouze et al., 2009; Dutay et al., 2009;
250 Kriest, 2002), which is similar to Rempfer et al., (2017) and Siddall et al., (2005).
251 Any particulate isotopes (A_p^i) at the ocean bottom layer are removed from the
252 ocean as sediment, which is the sink for the isotope budget. Detailed vertical
253 differentiation scheme to calculate this term in the model is provided in the
254 supplementary material. The reversible scavenging scheme applied here is the same
255 as the neodymium implementation in POP2 (Gu et al., 2017).

256
257 Therefore, the conservation equation for ^{231}Pa and ^{230}Th activity can be
258 written as

$$259 \quad \frac{\partial A_t^i}{\partial t} = \beta^i - \lambda^i A_t^i - w_s \frac{\partial A_p^i}{\partial z} + \text{Transport} \quad (3),$$

260 where the total isotope activity is controlled by decay from U (first term),
261 radioactive decay (second term), reversible scavenging (third term) and physical
262 transport by the ocean model (fourth term, including advection, convection and
263 diffusion). A_p^i can be calculated by combining Eq. (1) and Eq. (2):

264 $A_t^i = A_d^i + A_d^i \cdot (K_{POC}^i \cdot R_{POC} + K_{CaCO_3}^i \cdot R_{CaCO_3} + K_{opal}^i \cdot R_{opal})$
 265 $= A_d^i \cdot (1 + K_{POC}^i \cdot R_{POC} + K_{CaCO_3}^i \cdot R_{CaCO_3} + K_{opal}^i \cdot R_{opal}),$ (4)

266 which leads to

267 $A_d^i = \frac{A_t^i}{1 + K_{POC}^i \cdot R_{POC} + K_{CaCO_3}^i \cdot R_{CaCO_3} + K_{opal}^i \cdot R_{opal}},$ (5)

268 put this back to Eq. (1), we get

269 $A_p^i = A_t^i \cdot (1 - \frac{1}{1 + K_{POC}^i \cdot R_{POC} + K_{CaCO_3}^i \cdot R_{CaCO_3} + K_{opal}^i \cdot R_{opal}})$ (6)

270

271 Particle fields used in the reversible scavenging can be either prescribed or
 272 simultaneously generated from the marine ecosystem module. Therefore, two forms
 273 of ^{231}Pa and ^{230}Th are implemented in POP2: “p-fixed” and “p-coupled”. P-fixed ^{231}Pa
 274 and ^{230}Th use particle fluxes prescribed as annual mean particle fluxes generated
 275 from the marine ecosystem module under present day climate forcing (Fig.1). P-
 276 coupled ^{231}Pa and ^{230}Th use particle fluxes computed simultaneously from the
 277 marine ecosystem module. P-fixed and p-coupled ^{231}Pa and ^{230}Th can be turned on
 278 at the case build time and the p-coupled ^{231}Pa and ^{230}Th requires the ecosystem
 279 module to be turned on at the same time.

280

281 Comparing with previous studies of modeling ^{231}Pa and ^{230}Th , our p-fixed
 282 version is the same as Siddall et al., (2002), except that different prescribed particle
 283 fluxes are used. The p-coupled version allows coupling to biogeochemical module,
 284 which is similar to Rempfer et al., (2017), but we do not include boundary
 285 scavenging and sediment resuspensions as in Rempfer et al., (2017) because
 286 boundary scavenging and sediment resuspensions are suggested to be unimportant
 287 to influence the relationship between $^{231}\text{Pa}_p/^{230}\text{Th}_p$ and AMOC strength (Rempfer et
 288 al., 2017).

289

290 **3. Experiments**

291 We run a control experiment (CTRL) and two experiments with different
292 partition coefficients to show model sensitivity. We have both p-fixed and p-coupled
293 ^{231}Pa and ^{230}Th in CTRL, but only p-fixed ^{231}Pa and ^{230}Th in sensitivity experiments.
294 Equilibrium partition coefficients for ^{231}Pa and ^{230}Th vary among different particle
295 types and the magnitude of the partition coefficients for different particle types
296 remains uncertain (Chase et al., 2002; Chase and Robert F, 2004; Luo and Ku, 1999).
297 Since the control experiment in Siddall et al., (2005) is able to simulate major
298 features of ^{231}Pa and ^{230}Th distributions, we use the partition coefficients from the
299 control experiment in Siddall et al., (2005) in our CTRL (Table 2). Two sensitivity
300 experiments are performed with decreased (EXP_1) and increased (EXP_2) partition
301 coefficients by a factor of 5 (Table 2).

302 All the experiments are ocean-alone experiments with the normal year
303 forcing by CORE-II data (Large and Yeager, 2008). The ^{231}Pa and ^{230}Th activities are
304 initiated from 0 in CTRL and are integrated for 2,000 model years until equilibrium
305 is reached. EXP_1 and EXP_2 are initiated from 1,400 model year in CTRL and are
306 integrated for another 800 model years to reach equilibrium.

307 Since sediment $^{231}\text{Pa}/^{230}\text{Th}$ in North Atlantic has been used to reflect the
308 strength of AMOC, to test how sediment $^{231}\text{Pa}/^{230}\text{Th}$ in our model responds to the
309 change of AMOC and the change of particle fluxes, we carried out a fresh water
310 perturbation experiment (HOSING) with both p-fixed and p-coupled ^{231}Pa and ^{230}Th .
311 Starting from 2,000 model year of CTRL, a freshwater flux of 1 Sv is imposed over
312 the North Atlantic region of $50^\circ\text{N}\sim 70^\circ\text{N}$ and the experiment is integrated for 1400
313 model years until both p-fixed and p-coupled sediment $^{231}\text{Pa}/^{230}\text{Th}$ ratio have
314 reached quasi-equilibrium. The partition coefficients used in HOSING are the same
315 as in CTRL.

316

317 **4. Results**

318 4.1 Control Experiment

319 P-fixed and p-coupled version of ^{231}Pa and ^{230}Th in CTRL show identical
320 results (Fig. 2-4). P-fixed and p-coupled dissolved and particulate ^{231}Pa and ^{230}Th in
321 CTRL are highly correlated with each other with correlations greater than 0.995 and

322 regression coefficients are all near 1.0 ($R^2 > 0.995$). The correlation coefficient
323 between p-fixed and p-coupled sediment $^{231}\text{Pa}/^{230}\text{Th}$ activity ratios in CTRL is 0.99
324 and the regression coefficient is 0.9 ($R^2 = 0.98$). This is expected because the particle
325 fields used in p-fixed version are prescribed as the climatology of the particle fields
326 used in the p-coupled version. Therefore, under the same climate forcing, p-fixed
327 and p-coupled version of ^{231}Pa and ^{230}Th should be very similar. For the discussion
328 of results in CTRL below, we only discuss the p-fixed ^{231}Pa and ^{230}Th .

329 The residence time of both ^{231}Pa and ^{230}Th in CTRL are comparable with
330 observations. The residence time is calculated as the ratio of global average total
331 isotope activity and the radioactive ingrowth of the isotope. Residence time in CTRL
332 is 118 yr for ^{231}Pa and 33 yr for ^{230}Th (Table 2), which are of the same magnitude as
333 111 yr for ^{231}Pa and 26 yr for ^{230}Th in observation (Yu et al., 1996).

334 CTRL can simulate the general features of dissolved water column ^{231}Pa and
335 ^{230}Th activities. Dissolved ^{231}Pa and ^{230}Th activities increase with depth in CTRL, as
336 shown in two GEOTRACES transects (Deng et al., 2014; Hayes et al., 2015) in the
337 Atlantic (Fig. 2 and 3). The dissolved ^{231}Pa and ^{230}Th activities in CTRL are also at
338 the same order of magnitude as in observations in the most of the ocean, except that
339 simulated values are larger than observations in the abyssal, which is also the case
340 in Siddall et al., (2005) and Rempfer et al., (2017) (their Fig. 2 and 3, experiment
341 Re3d). Our model is unable to simulate the realistic dissolved ^{231}Pa and ^{230}Th
342 activities in the abyssal probably because boundary scavenging and sediment
343 resuspensions are not included in our model. In Rempfer et al., 2017, without
344 boundary scavenging and sediment resuspension, dissolved ^{231}Pa and ^{230}Th
345 activities are quite large in the deep ocean. However, if boundary scavenging and
346 sediment resuspension are included, the water column dissolved ^{231}Pa and ^{230}Th
347 activity is in the right magnitude compared with observation. Therefore, we hypothesize
348 that with boundary scavenging and sediment resuspensions added, dissolved ^{231}Pa
349 and ^{230}Th activities in the abyssal should be greatly reduced.

350 A more quantitative model-data comparison is shown in Fig. 5. The linear
351 regression coefficient between model results and observations (references of
352 observations are listed in Table 3), an indication of model ability to simulate ^{231}Pa

353 and ^{230}Th activity (Dutay et al., 2009), is near 1.0 for dissolved ^{231}Pa and ^{230}Th (1.02
354 for $[\text{}^{231}\text{Pa}]_d$ and 1.14 for $[\text{}^{230}\text{Th}]_d$), suggesting that CTRL can simulate the dissolved
355 ^{231}Pa and ^{230}Th in good agreement with observations. However, the simulation of
356 the particulate activity is not as good as the dissolved activity. Particulate activity is
357 overall larger than observation in the surface ocean and smaller than observation in
358 the deep ocean for both particulate ^{231}Pa and ^{230}Th . The regression coefficient for
359 particulate ^{231}Pa and ^{230}Th is 0.02 for $[\text{}^{231}\text{Pa}]_p$ and 0.05 for $[\text{}^{230}\text{Th}]_p$. The poor
360 performance in simulating water column particulate ^{231}Pa and ^{230}Th activities is also
361 in previous modeling studies (Dutay et al., 2009; Siddall et al., 2005), because of
362 similar modelling scheme applied. However, the simulated $^{231}\text{Pa}_p/^{230}\text{Th}_p$ is in
363 reasonable agreement with observations. The $^{231}\text{Pa}_p/^{230}\text{Th}_p$ along two GEOTRACES
364 transects (Fig. 2 and 3) show the similar pattern and magnitude as in Rempfer et al.,
365 (2017), consistent with observations. Decrease of $^{231}\text{Pa}_p/^{230}\text{Th}_p$ with depth is well
366 simulated, which is suggested to be caused by the lateral transport of ^{231}Pa from
367 North Atlantic to Southern Ocean by AMOC (Gherardi et al., 2009; Lippold et al.,
368 2011, 2012a; Luo et al., 2010; Rempfer et al., 2017).

369 The sediment $^{231}\text{Pa}/^{230}\text{Th}$ in CTRL is overall consistent with observations
370 (references of observations are listed in Table 3). The North Atlantic shows low
371 sediment $^{231}\text{Pa}/^{230}\text{Th}$ activity ratio as in observations because ^{231}Pa is more subject
372 to the southward transport by active ocean circulation than ^{230}Th because of its
373 longer residence time. The Southern Ocean maximum in the sediment $^{231}\text{Pa}/^{230}\text{Th}$
374 activity ratio is also simulated in CTRL. High opal fluxes in the Southern Ocean,
375 which preferentially removes ^{231}Pa into sediment ($K_{opal}^{231Pa} > K_{opal}^{230Th}$) (Chase et al.,
376 2002), leading to increased sediment $^{231}\text{Pa}/^{230}\text{Th}$ activity ratio. In addition,
377 upwelling in the Southern Ocean brings up deep water enriched with ^{231}Pa , which is
378 transported from the North Atlantic, to shallower depth and further contribute to
379 the scavenging. CTRL can also produce higher sediment $^{231}\text{Pa}/^{230}\text{Th}$ activity ratio in
380 regions with high particle production (e.g. the Eastern equatorial Pacific, the North
381 Pacific and the Indian Ocean) due to the “particle flux effect”. Specifically, in North
382 Atlantic, the distribution of sediment $^{231}\text{Pa}/^{230}\text{Th}$ matches the distribution of

383 particle, especially opal, production: sediment $^{231}\text{Pa}/^{230}\text{Th}$ is higher where opal
384 production is high, and vice versa (Fig. 4 and Fig. 1c). Quantitatively, the regression
385 coefficient between sediment $^{231}\text{Pa}/^{230}\text{Th}$ in CTRL and observation in the Atlantic is
386 0.86, which is larger than in other basins. This suggests that sediment $^{231}\text{Pa}/^{230}\text{Th}$ is
387 better simulated in the Atlantic than in other basins. One possible explanation is that
388 sediment $^{231}\text{Pa}/^{230}\text{Th}$ in the Atlantic is controlled by both ocean circulation and
389 particle flux, while in other basins sediment $^{231}\text{Pa}/^{230}\text{Th}$ is controlled almost only by
390 particle flux. With active AMOC, the north south gradient of sediment $^{231}\text{Pa}/^{230}\text{Th}$
391 can be simulated. However, for example, in the Southern Ocean, sediment
392 $^{231}\text{Pa}/^{230}\text{Th}$ is dominantly controlled by opal flux, which varies on small scales and is
393 difficult for simulation. Therefore, model performance in simulating sediment
394 $^{231}\text{Pa}/^{230}\text{Th}$ in the Southern Ocean is not as good as in the Atlantic.

395

396 4.2 Sensitivity on partition coefficient K

397 In this section, we show model sensitivity on partition coefficient by
398 increasing and decreasing the partition coefficient, K, by a factor of 5, but keeping
399 the relative ratio for different particles the same (Table 2). Our model shows similar
400 model sensitivity as in Siddall et al., (2005) as discussed below.

401 As stated in Siddall et al., (2005), the isotope decay term in Eq. (3) is three
402 orders of magnitude less than the production term. If we neglect the transport term
403 and the decay term in Eq. (3) and assume particulate phase activity at the surface as
404 0, when reach equilibrium, the activity of particulate phase will be as in Eq. (7). Eq.
405 (7) combined with Eq. (2) and $R_i = \frac{F}{w_s * \rho}$, we can obtain Eq. (8). Under the
406 assumption that there is isotope decay and ocean transport, Eq. (7) suggests that the
407 particulate isotope activity depends on the production rate and settling velocity and
408 will increase linearly with depth. Eq. (8) suggests that the dissolved isotope activity
409 depends on the production rate, partition coefficient K and particle flux and will also
410 increase linearly with depth. Any departure from this linear relationship with depth
411 is due to ocean transport, which is suggested by observations (Bacon and Anderson,

412 1982; Roy-Barman et al., 1996). Results of Eq. (7) and Eq. (8) can help to understand
413 the differences in Exp_1 and Exp_2.

414 Increasing K will decrease water column dissolved ^{231}Pa and ^{230}Th activities
415 but won't change particulate ^{231}Pa and ^{230}Th too much (Fig. 6). Magnitude of
416 dissolved ^{231}Pa and ^{230}Th in Exp_1 (smaller K) is at least one order larger than that
417 in Exp_2 (larger K), while magnitude of particulate ^{231}Pa and ^{230}Th in Exp_1 and
418 Exp_2 is in the same order. As suggested by Eq. (8), if there is no isotope decay and
419 no ocean transport, larger K will lead to smaller dissolved isotope activity but
420 unchanged particulate activity. Intuitively, larger K will lead to more ^{231}Pa and ^{230}Th
421 attached to particles and further buried into sediment, which increases the sink for
422 the ^{231}Pa and ^{230}Th budget. With the sources for ^{231}Pa and ^{230}Th staying the same,
423 dissolved ^{231}Pa and ^{230}Th will be reduced. Increasing K will also reduce the vertical
424 gradient of dissolved ^{231}Pa and ^{230}Th as reversible scavenging act as the vertical
425 transport and increase this vertical transport can decrease the vertical gradient.
426 However, changes in the particulate ^{231}Pa and ^{230}Th is relatively small (Fig. 6). Eq.
427 (7) suggests that particulate phase activity it is independent of K. Therefore,
428 changing K will have limited influence on particulate phase activity.

$$429 \quad A_p^i(z) = \frac{\beta^i}{w_s} \cdot z \quad (7)$$

$$430 \quad A_d^i(z) = \frac{\rho\beta^i}{K^i F} \cdot z \quad (8)$$

431
432 Increasing K will also reduce the spatial gradient in sediment $^{231}\text{Pa}/^{230}\text{Th}$
433 activity ratio and vice versa (Fig. 7). Larger K will decrease the ^{231}Pa and ^{230}Th
434 residence time and most isotopes produced in the water column are removed into
435 sediment locally (Table 2). Therefore, sediment $^{231}\text{Pa}/^{230}\text{Th}$ ratio becomes more
436 homogeneous and approaching the production ration of 0.093 (Fig. 7b). The
437 deviation (the root mean squared error) of sediment $^{231}\text{Pa}/^{230}\text{Th}$ is 0.0726 in CTRL,
438 0.0770 in Exp_1 and 0.0739 in Exp_2. The linear regression coefficients between
439 sediment $^{231}\text{Pa}/^{230}\text{Th}$ in the model and the observations are listed in Table S1 in the

440 supplementary information. Although the performance of global sediment
441 $^{231}\text{Pa}/^{230}\text{Th}$ in Exp_1 is better than CTRL, the performance of Atlantic $^{231}\text{Pa}/^{230}\text{Th}$ in
442 Exp_1 is worse. We consider better simulating sediment $^{231}\text{Pa}/^{230}\text{Th}$ in the Atlantic
443 is more important since the most important application of sediment $^{231}\text{Pa}/^{230}\text{Th}$ is
444 using sediment $^{231}\text{Pa}/^{230}\text{Th}$ in the North Atlantic to reconstruct past AMOC. In
445 addition, water column isotope activity is too large in Exp_1 compared with
446 observation. Therefore, the partition coefficient in CTRL is of the right order of
447 magnitude.

448

449 4.3. Sediment $^{231}\text{Pa}/^{230}\text{Th}$ ratio in HOSING

450 Potential changes in the export of biogenic particles makes using $^{231}\text{Pa}/^{230}\text{Th}$
451 ratio to reconstruct AMOC strength under debate. In response to freshwater
452 perturbation in the North Atlantic, both biological productivity and AMOC strength
453 will change and will influence sediment $^{231}\text{Pa}/^{230}\text{Th}$ in different ways. Our model
454 with p-fixed and p-coupled ^{231}Pa and ^{230}Th can help to detangle these two effects. In
455 this section, we examine the sediment $^{231}\text{Pa}/^{230}\text{Th}$ (p-fixed and p-coupled) response
456 in the North Atlantic to idealized fresh water perturbation.

457 In HOSING, after applying freshwater forcing to the North Atlantic, AMOC
458 strength quickly decreases to a minimum of 2 Sv (AMOC_off) (Fig. 9a). During the
459 AMOC_off state, compared with CTRL with active AMOC (AMOC_on), p-fixed
460 sediment $^{231}\text{Pa}/^{230}\text{Th}$ shows an overall increase in the North Atlantic and a decrease
461 in the South Atlantic (Fig. 10b) because of the reduced southward transport of ^{231}Pa
462 from the North Atlantic by AMOC, consistent with paleo proxy evidence there (e.g.
463 Gherardi et al., 2005, 2009; McManus et al., 2004). The overall increase of sediment
464 $^{231}\text{Pa}/^{230}\text{Th}$ ratio in the North Atlantic in response to the AMOC collapse can be seen
465 more clearly in the time evolution of the sediment $^{231}\text{Pa}/^{230}\text{Th}$ ratio averaged from
466 20°N to 60°N in the North Atlantic (Fig.9b, green). Quantitatively, the $^{231}\text{Pa}/^{230}\text{Th}$
467 increases from 0.074 in AMOC_on to 0.098 in AMOC_off in the p-fixed version,
468 approaching the production ration of 0.093. This increase of $^{231}\text{Pa}/^{230}\text{Th}$ is also in
469 the subtropical North Atlantic from the two sites near Bermuda Rise (Fig. 9e and f),
470 which is of comparable magnitude with the change from LGM to HS1 in

Deleted: ing

472 reconstructions there (McManus et al., 2004). In addition, the pattern of p-fixed
473 (Fig.10a) sediment $^{231}\text{Pa}/^{230}\text{Th}$ ratio during the Atlantic in AMOC_off state is similar
474 to the opal distribution (Fig.1b) because, without active circulation, sediment
475 $^{231}\text{Pa}/^{230}\text{Th}$ ratio is more controlled by particle flux effect, which is similar to the
476 Pacific in CTRL. It is further noted that our p-fixed sediment $^{231}\text{Pa}/^{230}\text{Th}$ ratio in
477 HOSING behaves similarly to that in Siddall et al., (2007).

478 The overall increase in p-fixed sediment $^{231}\text{Pa}/^{230}\text{Th}$ ratio in the North
479 Atlantic is not homogenous and the magnitude of the change between AMOC_on and
480 AMOC_off varies with location, depending on the distribution of particle flux,
481 especially the opal flux (Fig.9 and 10). The maximum increase in p-fixed sediment
482 $^{231}\text{Pa}/^{230}\text{Th}$ ratio occurs near 40°N western Atlantic (Fig. 10a), where the opal
483 production in our model is maximum in North Atlantic (Fig. 1b). The sediment
484 $^{231}\text{Pa}/^{230}\text{Th}$ ratio in this region during AMOC_on is larger than production ratio of
485 0.093 because opal maximum provides extra ^{231}Pa to this region (“particle flux
486 effect”), which overwhelms the active ocean circulation transporting ^{231}Pa
487 southward outside this region (Fig. 9d, green). During AMOC_off, without active
488 ocean circulation, the particle flux effect becomes even stronger because less ^{231}Pa is
489 transported out of the North Atlantic and p-fixed sediment $^{231}\text{Pa}/^{230}\text{Th}$ ratio
490 becomes even larger. It should be noted that the opal maximum in this region is not
491 in the observation (Fig. 7.2.5 in Sarmiento and Gruber 2006). However, our
492 sediment $^{231}\text{Pa}/^{230}\text{Th}$ response in HOSING is self-consistent with the particle flux in
493 our model since the location of maximum $^{231}\text{Pa}/^{230}\text{Th}$ increase matches the location
494 of opal flux in our model.

495 In most regions of the Atlantic, p-coupled sediment $^{231}\text{Pa}/^{230}\text{Th}$ shows a
496 similar response to p-fixed $^{231}\text{Pa}/^{230}\text{Th}$ in HOSING. The evolution of p-fixed and p-
497 coupled sediment $^{231}\text{Pa}/^{230}\text{Th}$ activity ratio in HOSING are highly correlated (Fig.
498 11a). The change of sediment $^{231}\text{Pa}/^{230}\text{Th}$ ratio from AMOC_on to AMOC_off are
499 similar in both the p-fixed and p-coupled version (Fig.11b). The correlation between
500 p-fixed and p-coupled sediment $^{231}\text{Pa}/^{230}\text{Th}$ ratio change from AMOC_on to
501 AMOC_off is 0.72 (1455points) and the linear regression coefficient is 0.71 ($R^2 =$
502 0.52). A high correlation between p-fixed and p-coupled response mainly happens

Deleted: ,

Deleted: H

505 over low productivity regions (Fig.1, 10, and 11), where circulation effect on
506 sediment $^{231}\text{Pa}/^{230}\text{Th}$ is more important than the particle flux change in HOSING.

507 In spite of these similarities discussed above, the responses of p-fixed and p-
508 coupled sediment $^{231}\text{Pa}/^{230}\text{Th}$ to the fresh water forcing can differ significantly in
509 high productivity regions because of the productivity change. With persistent
510 freshwater forcing over the North Atlantic, most regions in the North Atlantic show
511 reduced production of CaCO_3 , opal and POC (Fig. 8). Productivity in the North
512 Atlantic is suggested to be halved during AMOC collapse because of increased
513 stratification, which reduces nutrient supply from deep ocean (Schmittner, 2005). In
514 our model, the productivity in the mid-latitude North Atlantic is indeed greatly
515 reduced after the freshwater forcing is applied. For example, opal production from
516 30°N - 50°N in the Atlantic at the end of HOSING is reduced by 50%~90% of its
517 original value in CTRL. However, opal production increases in high latitude North
518 Atlantic (north of 50°N). The pattern of opal production changes with high opal
519 production region shifts northward in HOSING (Fig. 8 d, e and f). These particle flux
520 changes will influence sediment $^{231}\text{Pa}/^{230}\text{Th}$ as discussed below.

521 North of 50°N in the Atlantic, ~~opal productivity increases during AMOC_off~~
522 (Fig. 8f) and will result an increase in sediment $^{231}\text{Pa}/^{230}\text{Th}$. The increase caused by
523 greater opal productivity enhances the sediment $^{231}\text{Pa}/^{230}\text{Th}$ increase caused by
524 reduced AMOC. Therefore, the increase in p-coupled sediment $^{231}\text{Pa}/^{230}\text{Th}$ from
525 AMOC_on to AMOC_off is larger than p-fixed sediment $^{231}\text{Pa}/^{230}\text{Th}$ change (Fig.9c).

Deleted: the

526 In the mid-latitude North Atlantic, ~~opal productivity decreases during~~
527 AMOC_off (Fig.8 f) and will lead to a decrease in sediment $^{231}\text{Pa}/^{230}\text{Th}$, which is
528 opposite to the effect of reduced AMOC. P-coupled sediment $^{231}\text{Pa}/^{230}\text{Th}$ shows an
529 initial decrease in first 200 years (Fig.9 d, e, and f, red dash lines) caused by the
530 reduced opal productivity. But this decrease trend is reversed eventually, suggesting
531 that the influence of particle flux change is overwhelmed by the effect of reduced
532 AMOC. In the long run, most regions in the subtropical and mid-latitude Atlantic
533 show increased sediment $^{231}\text{Pa}/^{230}\text{Th}$ in HOSING (Fig.10 d), indicating the dominant
534 effect of reduced AMOC. However, sediment $^{231}\text{Pa}/^{230}\text{Th}$ at 40°N west Atlantic,
535 where opal productivity is maximum during AMOC_on, show a decrease from

Deleted: the

538 AMOC_on to AMOC_off (Fig.9 d and Fig.10 d). During AMOC_on, the opal productivity
539 maximum at 40°N west Atlantic lead to regional maximum sediment $^{231}\text{Pa}/^{230}\text{Th}$
540 because of the particle flux effect (Fig. 4). During AMOC_off, this opal productivity
541 maximum is eliminated (Fig.8 e) and there is no more extra ^{231}Pa supplied by
542 surroundings to this region, which leads to a decrease in sediment $^{231}\text{Pa}/^{230}\text{Th}$. This
543 decrease in sediment $^{231}\text{Pa}/^{230}\text{Th}$ caused by productivity change is greater than the
544 increase caused by the reduced AMOC. Therefore, sediment $^{231}\text{Pa}/^{230}\text{Th}$ experiences
545 a decrease from AMOC_on to AMOC_off at this location (Fig.9 d and Fig.10 d). Our
546 results suggest that although the circulation effect is more dominant than the
547 particle flux change in controlling sediment $^{231}\text{Pa}/^{230}\text{Th}$ on long time scale over
548 most of North Atlantic (Fig. 11), particle flux change can be important on short time
549 scale and in high productivity regions. With p-fixed and p-coupled ^{231}Pa and ^{230}Th ,
550 our model can help to detangle the circulation effect and particle flux effect.

551

552 It has been suggested that the particulate $^{231}\text{Pa}/^{230}\text{Th}$ response to the change
553 of AMOC depends on the location and depth. Above 2km and high latitude North
554 Atlantic, particulate $^{231}\text{Pa}/^{230}\text{Th}$ decreases with the increased AMOC (Rempfer et al.,
555 2017). Our results are consistent with this finding (Fig. 12 a and b). Both p-fixed and
556 p-coupled particulate $^{231}\text{Pa}/^{230}\text{Th}$ show similar patterns of change from AMOC_on to
557 AMOC_off: decrease in particulate $^{231}\text{Pa}/^{230}\text{Th}$ at shallow depth and north of 60°N
558 and increase in particulate $^{231}\text{Pa}/^{230}\text{Th}$ below 2km and south of 60°N during
559 AMOC_off. Therefore, sediment depth should also be taken into consideration when
560 interpreting sediment $^{231}\text{Pa}/^{230}\text{Th}$. Since the pattern in p-coupled is similar to the
561 pattern in p-fixed, the opposite particulate $^{231}\text{Pa}/^{230}\text{Th}$ changes in shallow and deep
562 North Atlantic is associated with AMOC change. During AMOC_on, upper limb of
563 AMOC (about upper 1km) transport water northward, which provides extra ^{231}Pa to
564 North Atlantic and particulate $^{231}\text{Pa}/^{230}\text{Th}$ is larger than the production ratio of
565 0.093. In contrast, the lower limb of AMOC (2km-3km) features southward
566 transport, which transports ^{231}Pa to the Southern Ocean and particulate $^{231}\text{Pa}/^{230}\text{Th}$
567 is smaller than the production ratio of 0.093 (Fig. 12 solid). Particulate $^{231}\text{Pa}/^{230}\text{Th}$
568 decreases with depth (Fig. 12 c solid). During AMOC_off, ocean transport of ^{231}Pa is

569 greatly reduced. Therefore, shallow (deep) depth experiences a decrease (increase)
570 in particulate $^{231}\text{Pa}/^{230}\text{Th}$ and the vertical gradient in the particulate $^{231}\text{Pa}/^{230}\text{Th}$ is
571 also greatly reduced (Fig. 12 c dash). Our results support that the depth dependence
572 of particulate $^{231}\text{Pa}/^{230}\text{Th}$ is mainly caused by lateral transport of ^{231}Pa by
573 circulation (Gherardi et al., 2009; Lippold et al., 2011, 2012a; Luo et al., 2010;
574 Rempfer et al., 2017).

575 Overall, our model is able to simulate the correct magnitude of the sediment
576 $^{231}\text{Pa}/^{230}\text{Th}$ ratio response to the freshwater forcing. Our experiments suggest that
577 the change of circulation is the dominant factor that influences sediment $^{231}\text{Pa}/^{230}\text{Th}$
578 on long time scale over most of the globe in the idealized hosing experiment,
579 although the detailed difference between p-fixed and p-coupled sediment
580 $^{231}\text{Pa}/^{230}\text{Th}$ ratio response to freshwater forcing in different locations can be
581 complicated.

582

583

584 **5. Summary**

585 ^{231}Pa and ^{230}Th have been implemented in the ocean model of the CESM in
586 both the p-coupled and p-fixed forms. Our control experiment under present day
587 climate forcing is able to simulate most ^{231}Pa and ^{230}Th water column activity and
588 sediment $^{231}\text{Pa}/^{230}\text{Th}$ activity ratio consistent with observations by using the
589 parameters that are suggested by Chase et al., (2002) and used in Siddall et al.
590 (2005). Our sensitivity experiments with varying parameters suggest that these
591 parameters are of the right order of magnitude.

592 Furthermore, our model is able to simulate the overall sediment $^{231}\text{Pa}/^{230}\text{Th}$
593 ratio change in the North Atlantic with a magnitude comparable to the
594 reconstruction in response to the collapse of AMOC, although the detailed response
595 can be complicated in different regions. Finally, the p-fixed form is able to capture
596 many major features of that of the p-coupled form over large ocean areas on long
597 time scale, although the two forms can also differ significantly in some regions,
598 especially the region with high opal productivity.

599 Much remains to be improved in our ^{231}Pa and ^{230}Th module in the future.
600 For example, the model can be further improved by including nepheloid layers to
601 better simulate water column ^{231}Pa and ^{230}Th activity as in Rempfer et al. (2017). In
602 addition, partition coefficient for different particles can be further tuned , which can
603 improve our understanding of the affinity of ^{231}Pa and ^{230}Th to different particles,
604 complementing the limited observational studies available (e.g. Chase et al., 2002;
605 Scholten et al., 2005; Walter et al., 1997). At present, as the first attempt to implement
606 ^{231}Pa and ^{230}Th in the CESM with both p-fixed and p-coupled versions, our model
607 can serve as a useful tool to improve our understanding of the processes of ^{231}Pa
608 and ^{230}Th as well as interpretations of sediment $^{231}\text{Pa}/^{230}\text{Th}$ reconstructions for past
609 ocean circulation and climate changes.

610

611

612 **Code availability:**

613 The ^{231}Pa and ^{230}Th isotope source code of both p-fixed and p-coupled versions for
614 CESM1.3 is included as supplementary material here.

615

616

617 **Acknowledgement:**

618 This work is supported by NSF P2C2 program (NSF 1401778 and NSF1600080),
619 DOE DE-SC0006744 and NSFC 41630527 and 41130105. Computing resources
620 (ark:/85065/d7wd3xhc) were provided by the Climate Simulation Laboratory at
621 NCAR's Computational and Information Systems Laboratory, sponsored by the
622 National Science Foundation and other agencies.

623

624 **References:**

625 Anderson, R. F., Bacon, M. P. and Brewer, P. G.: Removal of ^{230}Th and ^{231}Pa from the
626 open ocean, *Earth Planet. Sci. Lett.*, 62(1), 7–23, doi:10.1016/0012-821X(83)90067-
627 5, 1983.
628 Anderson, R. F., Lao, Y., Broecker, W. S., Trumbore, S. E., Hofmann, H. J. and Wolfli, W.:
629 Boundary scavenging in the Pacific Ocean: A comparison of ^{10}Be and ^{231}Pa , *Earth*
630 *Planet. Sci. Lett.*, 96(3–4), 287–304, doi:10.1016/j.cognition.2008.05.007, 1990.
631 Anderson, R. F., Fleisher, M. Q., Biscaye, P. E., Kumar, N., Dittrich, B., Kubik, P. and
632 Suter, M.: Anomalous boundary scavenging in the Middle Atlantic Bight: evidence

633 from ^{230}Th , ^{231}Pa , ^{10}Be and ^{210}Pb , *Deep. Res. Part II*, 41(2-3), 537-561,
634 doi:10.1016/0967-0645(94)90034-5, 1994.
635 Armstrong, R. A., Lee, C., Hedges, J. I., Honjo, S. and Wakeham, S. G.: A new,
636 mechanistic model for organic carbon fluxes in the ocean based on the quantitative
637 association of POC with ballast minerals, *Deep. Res. Part II Top. Stud. Oceanogr.*,
638 49(1-3), 219-236, doi:10.1016/S0967-0645(01)00101-1, 2002.
639 Arsouze, T., Dutay, J.-C., Lacan, F. and Jeandel, C.: Reconstructing the Nd oceanic
640 cycle using a coupled dynamical - biogeochemical model, *Biogeosciences*, 6(12),
641 2829-2846, doi:10.5194/bg-6-2829-2009, 2009.
642 Bacon, M. and Anderson, R.: Distribution of Thorium Isotopes between dissolved
643 and particulate forms in the deep sea, *J. Geophys. Res. ...*, 87(1), 2045-2056, 1982.
644 Bacon, M. P. and Rosholt, J. N.: Accumulation rates of ^{230}Th , ^{231}Pa , and some
645 transition metals on the Bermuda Rise, *Geochim. Cosmochim. Acta*, 46, 651-666,
646 1982.
647 Bacon, M. P., Huh, C. A. and Moore, R. M.: Vertical profiles of some natural
648 radionuclides over the Alpha Ridge, Arctic Ocean, *Earth Planet. Sci. Lett.*, 95(1-2),
649 15-22, doi:10.1016/0012-821X(89)90164-7, 1989.
650 Bradtmiller, L. I., Anderson, R. F., Fleisher, M. Q. and Burckle, L. H.: Opal burial in the
651 equatorial Atlantic Ocean over the last 30 ka: Implications for glacial-interglacial
652 changes in the ocean silicon cycle, *Paleoceanography*, 22(4), 1-15,
653 doi:10.1029/2007PA001443, 2007.
654 Bradtmiller, L. I., McManus, J. F. and Robinson, L. F.: $^{231}\text{Pa}/^{230}\text{Th}$ evidence for a
655 weakened but persistent Atlantic meridional overturning circulation during
656 Heinrich Stadial 1, *Nat. Commun.*, 5, 5817, doi:10.1038/ncomms6817, 2014.
657 Burckel, P., Waelbroeck, C., Luo, Y., Roche, D. M., Pichat, S., Jaccard, S. L., Gherardi, J.,
658 Govin, A., Lippold, J. and Thil, F.: Changes in the geometry and strength of the
659 Atlantic meridional overturning circulation during the last glacial (20-50 ka), *Clim.*
660 *Past*, 12(11), 2061-2075, doi:10.5194/cp-12-2061-2016, 2016.
661 Chase, Z. and Robert F, A.: Comment on "On the importance of opal, carbonate, and
662 lithogenic clays in scavenging and fractionating ^{230}Th , ^{231}Pa and ^{10}Be in the ocean"
663 by S. Luo and T.-L. Ku, *Earth Planet. Sci. Lett.*, 220(1-2), 201-211,
664 doi:10.1016/S0012-821X(04)00027-5, 2004.
665 Chase, Z., Anderson, R. F., Fleisher, M. Q. and Kubik, P. W.: The influence of particle
666 composition and particle flux on scavenging of Th, Pa and Be in the ocean, *Earth*
667 *Planet. Sci. Lett.*, 204(1-2), 215-229, doi:10.1016/S0012-821X(02)00984-6, 2002.
668 Cochran, J. K., Livingston, H. D., Hirschberg, D. J. and Surprenant, L. D.: Natural and
669 anthropogenic radionuclide distributions in the northwest Atlantic Ocean, *Earth*
670 *Planet. Sci. Lett.*, 84(2-3), 135-152, doi:10.1016/0012-821X(87)90081-1, 1987.
671 Cochran, J. K., Hirschberg, D. J., Livingston, H. D., Buesseler, K. O. and Key, R. M.:
672 Natural and anthropogenic radionuclide distributions in the Nansen Basin, Arctic
673 Ocean: Scavenging rates and circulation timescales, *Deep. Res. Part II*, 42(6), 1495-
674 1517, doi:10.1016/0967-0645(95)00051-8, 1995.
675 Colley, S., Thomson, J. and Newton, P. P.: Detailed Th-230, Th-232 and Pb-210 fluxes
676 recorded by the 1989/90 BOFS sediment trap time-series at 48N, 20W, *Deep - Sea*
677 *Res. Part I - Oceanogr. Res. Pap.*, 42(6), 833-848, 1995.
678 Coppola, L., Roy-Barman, M., Mulsow, S., Povinec, P. and Jeandel, C.: Thorium

679 isotopes as tracers of particles dynamics and deep water circulation in the Indian
680 sector of the Southern Ocean (ANTARES IV), *Mar. Chem.*, 100(3–4 SPEC. ISS.), 299–
681 313, doi:10.1016/j.marchem.2005.10.019, 2006.

682 Danabasoglu, G., Bates, S. C., Briegleb, B. P., Jayne, S. R., Jochum, M., Large, W. G.,
683 Peacock, S. and Yeager, S. G.: The CCSM4 ocean component, *J. Clim.*, 25(5), 1361–
684 1389, doi:10.1175/JCLI-D-11-00091.1, 2012.

685 DeMaster, D. J.: The marine budgets of silica and ^{32}Si , Yale., 1979.

686 Deng, F., Thomas, A. L., Rijkenberg, M. J. A. and Henderson, G. M.: Controls on
687 seawater ^{231}Pa , ^{230}Th and ^{232}Th concentrations along the flow paths of deep
688 waters in the Southwest Atlantic, *Earth Planet. Sci. Lett.*, 390, 93–102,
689 doi:10.1016/j.epsl.2013.12.038, 2014.

690 Doney, S. C., Lima, I., Feely, R. A., Glover, D. M., Lindsay, K., Mahowald, N., Moore, J. K.
691 and Wanninkhof, R.: Mechanisms governing interannual variability in upper-ocean
692 inorganic carbon system and air-sea CO_2 fluxes: Physical climate and atmospheric
693 dust, *Deep. Res. Part II Top. Stud. Oceanogr.*, 56(8–10), 640–655,
694 doi:10.1016/j.dsr2.2008.12.006, 2009.

695 Dutay, J.-C., Lacan, F., Roy-Barman, M. and Bopp, L.: Influence of particle size and
696 type on ^{231}Pa and ^{230}Th simulation with a global coupled biogeochemical-ocean
697 general circulation model: A first approach, *Geochemistry, Geophys. Geosystems*,
698 10(1), doi:10.1029/2008GC002291, 2009.

699 Edmonds, H. N., Moran, S. B., Hoff, J. A., Smith, J. N. and Edwards, R. L.: Protactinium-
700 ^{231}Pa and Thorium- ^{230}Th Abundances and High Scavenging Rates in the Western Arctic
701 Ocean, *Science* (80-.), 280(5362), 405–407, doi:10.1126/science.280.5362.405,
702 1998.

703 Edmonds, H. N., Moran, S. B., Cheng, H. and Edwards, R. L.: ^{230}Th and ^{231}Pa in the
704 Arctic Ocean: Implications for particle fluxes and basin-scale Th/Pa fractionation,
705 *Earth Planet. Sci. Lett.*, 227(1–2), 155–167, doi:10.1016/j.epsl.2004.08.008, 2004.

706 Francois, R., Bacon, M. P., Altabet, M. A. and Labeyrie, L. D.: Glacial/interglacial
707 changes in sediment rain rate in the SW Indian Sector of subantarctic Waters as
708 recorded by ^{230}Th , ^{231}Pa , U, and $\delta^{15}\text{N}$, *Paleoceanography*, 8(5), 611–629,
709 doi:10.1029/93PA00784, 1993.

710 Frank, M.: Reconstruction of Late Quaternary environmental conditions applying the
711 natural radionuclides ^{230}Th , ^{10}Be , ^{231}Pa and ^{238}U : A study of deep-sea sediments
712 from the eastern sector of the Antarctic Circumpolar Current System, Alfred
713 Wegener Institute for Polar and Marine Research., 1996.

714 Frank, M., Eisenhauer, A., Kubik, P. W., Dittrich-hannen, B. and Segl, M.: Beryllium 10,
715 thorium 230, and protactinium 231 in Galapagos microplate sediments:
716 Implications of hydrothermal activity and paleoproductivity changes during the last
717 100,000 years, *Palaeogeography*, 9(4), 559–578, 1994.

718 Geibert, W. and Usbeck, R.: Adsorption of thorium and protactinium onto different
719 particle types: Experimental findings, *Geochim. Cosmochim. Acta*, 68(7), 1489–1501,
720 doi:10.1016/j.gca.2003.10.011, 2004.

721 Gherardi, J., Labeyrie, L., Mcmanus, J., Francois, R., Skinner, L. and Cortijo, E.:
722 Evidence from the Northeastern Atlantic basin for variability in the rate of the
723 meridional overturning circulation through the last deglaciation, *Earth Planet. Sci.*
724 *Lett.*, 240(3–4), 710–723, doi:10.1016/j.epsl.2005.09.061, 2005.

725 Gherardi, J.-M., Labeyrie, L., Nave, S., Francois, R., McManus, J. F. and Cortijo, E.:
726 Glacial-interglacial circulation changes inferred from $^{231}\text{Pa}/^{230}\text{Th}$ sedimentary
727 record in the North Atlantic region, *Paleoceanography*, 24(2),
728 doi:10.1029/2008PA001696, 2009.

729 Gu, S., Liu, Z., Zhang, J., Rempfer, J., Joos, J., Brady, E. and Oppo, D.: Coherent response
730 of Antarctic Intermediate Water and Atlantic Meridional Overturning Circulation
731 during the last deglaciation, *Palaeogeography*, doi:10.1002/2017PA003092, 2017.

732 Guo, L., Santschi, P. H., Baskaran, M. and Zindler, A.: Distribution of dissolved and
733 particulate ^{230}Th and ^{232}Th in seawater from the Gulf of Mexico and off Cape
734 Hatteras as measured by SIMS, *Earth Planet. Sci. Lett.*, 133(1), 117–128, 1995.

735 Gutjahr, M., Frank, M., Stirling, C. H., Keigwin, L. D. and Halliday, a. N.: Tracing the Nd
736 isotope evolution of North Atlantic Deep and Intermediate Waters in the western
737 North Atlantic since the Last Glacial Maximum from Blake Ridge sediments, *Earth
738 Planet. Sci. Lett.*, 266(1–2), 61–77, doi:10.1016/j.epsl.2007.10.037, 2008.

739 Hall, I. R., Moran, S. B., Zahn, R., Knutz, P. C., Shen, C.-C. and Edwards, R. L.:
740 Accelerated drawdown of meridional overturning in the late-glacial Atlantic
741 triggered by transient pre-H event freshwater perturbation, *Geophys. Res. Lett.*,
742 33(16), L16616, doi:10.1029/2006GL026239, 2006.

743 Hayes, C. T., Anderson, R. F., Fleisher, M. Q., Serno, S., Winckler, G. and Gersonde, R.:
744 Quantifying lithogenic inputs to the North Pacific Ocean using the long-lived
745 thorium isotopes, *Earth Planet. Sci. Lett.*, 383, 16–25,
746 doi:10.1016/j.epsl.2013.09.025, 2013.

747 Hayes, C. T., Anderson, R. F., Fleisher, M. Q., Huang, K. F., Robinson, L. F., Lu, Y., Cheng,
748 H., Edwards, R. L. and Moran, S. B.: ^{230}Th and ^{231}Pa on GEOTRACES GA03, the U.S.
749 GEOTRACES North Atlantic transect, and implications for modern and
750 paleoceanographic chemical fluxes, *Deep. Res. Part II Top. Stud. Oceanogr.*, 116, 29–
751 41, doi:10.1016/j.dsr2.2014.07.007, 2015.

752 Henderson, G. M. and Anderson, R. F.: The U-series toolbox for paleoceanography,
753 *Rev. Mineral. Geochemistry*, 52(1), 493–531, doi:10.2113/0520493, 2003.

754 Henderson, G. M., Heinze, C., Anderson, R. F. and Winguth, A. M. E.: Global
755 distribution of the ^{230}Th flux to ocean sediments constrained by GCM modelling,
756 *Deep. Res. Part I Oceanogr. Res. Pap.*, 46(11), 1861–1893, doi:10.1016/S0967-
757 0637(99)00030-8, 1999.

758 Hoffmann, S. S., McManus, J. F., Curry, W. B. and Brown-Leger, L. S.: Persistent export
759 of ^{231}Pa from the deep central Arctic Ocean over the past 35,000 years., *Nature*,
760 497(7451), 603–6, doi:10.1038/nature12145, 2013.

761 Hsieh, Y. Te, Henderson, G. M. and Thomas, A. L.: Combining seawater ^{232}Th and
762 ^{230}Th concentrations to determine dust fluxes to the surface ocean, *Earth Planet.
763 Sci. Lett.*, 312(3–4), 280–290, doi:10.1016/j.epsl.2011.10.022, 2011.

764 Huh, C. A. and Beasley, T. M.: Profiles of dissolved and particulate thorium isotopes
765 in the water column of coastal Southern California, *Earth Planet. Sci. Lett.*, 85(1–3),
766 1–10, doi:10.1016/0012-821X(87)90016-1, 1987.

767 Hurrell, J. W., Holland, M. M., Gent, P. R., Ghan, S., Kay, J. E., Kushner, P. J., Lamarque, J.
768 F., Large, W. G., Lawrence, D., Lindsay, K., Lipscomb, W. H., Long, M. C., Mahowald, N.,
769 Marsh, D. R., Neale, R. B., Rasch, P., Vavrus, S., Vertenstein, M., Bader, D., Collins, W. D.,
770 Hack, J. J., Kiehl, J. and Marshall, S.: The community earth system model: A

771 framework for collaborative research, *Bull. Am. Meteorol. Soc.*, 94(9), 1339–1360,
772 doi:10.1175/BAMS-D-12-00121.1, 2013.

773 Jahn, A., Lindsay, K., Giraud, X., Gruber, N., Otto-Bliesner, B. L., Liu, Z. and Brady, E. C.:
774 Carbon isotopes in the ocean model of the Community Earth System Model (CESM1),
775 *Geosci. Model Dev.*, 8(8), 2419–2434, doi:10.5194/gmd-8-2419-2015, 2015.

776 Jonkers, L., Zahn, R., Thomas, A., Henderson, G., Abouchami, W., Francois, R.,
777 Masque, P., Hall, I. R. and Bickert, T.: Deep circulation changes in the central South
778 Atlantic during the past 145 kyrs reflected in a combined $^{231}\text{Pa}/^{230}\text{Th}$,
779 Neodymium isotope and benthic $\delta^{13}\text{C}$ record, *Earth Planet. Sci. Lett.*, 419, 14–21,
780 doi:10.1016/j.epsl.2015.03.004, 2015.

781 Keigwin, L. D. and Boyle, E. A.: Did North Atlantic overturning halt 17,000 years ago?,
782 *Paleoceanography*, 23(1), 1–5, doi:10.1029/2007PA001500, 2008.

783 Kriest, I.: Different parameterizations of marine snow in a 1D-model and their
784 influence on representation of marine snow, nitrogen budget and sedimentation,
785 *Deep. Res. Part I Oceanogr. Res. Pap.*, 49(12), 2133–2162, doi:10.1016/S0967-
786 0637(02)00127-9, 2002.

787 Ku, T. L.: Uranium series disequilibrium in deep sea sediments, Columbia., 1966.

788 Ku, T. L., Bischoff, J. L. and Boersma, A.: Age studies of Mid-Atlantic Ridge sediments
789 near 42°N and 20°N , *Deep. Res. Oceanogr. Abstr.*, 19(3), 233–247,
790 doi:10.1016/0011-7471(72)90033-2, 1972.

791 Kumar, N.: Trace metals and natural radionuclides as tracers of ocean productivity,
792 Columbia., 1994.

793 Kumar, N., Gwiazda, R., Anderson, R. F. and Froelich, P. N.: $^{231}\text{Pa}/^{230}\text{Th}$ ratios in
794 sediments as a proxy for past changes in Southern Ocean productivity, *Nature*, 362,
795 45–48, doi:10.1038/362045a0, 1993.

796 Large, W. G. and Yeager, S. G.: The global climatology of an interannually varying air-
797 sea flux data set, *Clim. Dyn.*, 33(2–3), 341–364, doi:10.1007/s00382-008-0441-3,
798 2008.

799 Lippold, J., Grützner, J., Winter, D., Lahaye, Y., Mangini, A. and Christl, M.: Does
800 sedimentary $^{231}\text{Pa}/^{230}\text{Th}$ from the Bermuda Rise monitor past Atlantic Meridional
801 Overturning Circulation?, *Geophys. Res. Lett.*, 36(12), 1–6,
802 doi:10.1029/2009GL038068, 2009.

803 Lippold, J., Gherardi, J. M. and Luo, Y.: Testing the $^{231}\text{Pa}/^{230}\text{Th}$ paleocirculation proxy:
804 A data versus 2D model comparison, *Geophys. Res. Lett.*, 38(20), 1–7,
805 doi:10.1029/2011GL049282, 2011.

806 Lippold, J., Mulitza, S., Mollenhauer, G., Weyer, S., Heslop, D. and Christl, M.:
807 Boundary scavenging at the East Atlantic margin does not negate use of $^{231}\text{Pa}/$
808 ^{230}Th to trace Atlantic overturning, *Earth Planet. Sci. Lett.*, 333–334, 317–331,
809 doi:10.1016/j.epsl.2012.04.005, 2012a.

810 Lippold, J., Luo, Y., Francois, R., Allen, S. E., Gherardi, J., Pichat, S., Hickey, B. and
811 Schulz, H.: Strength and geometry of the glacial Atlantic Meridional Overturning
812 Circulation, *Nat. Geosci.*, 5(11), 813–816, doi:10.1038/ngeo1608, 2012b.

813 Long, M. C., Lindsay, K., Peacock, S., Moore, J. K. and Doney, S. C.: Twentieth-century
814 oceanic carbon uptake and storage in CESM1(BGC), *J. Clim.*, 26(18), 6775–6800,
815 doi:10.1175/JCLI-D-12-00184.s1, 2013.

816 Luo, S. and Ku, T. L.: Oceanic $^{231}\text{Pa}/^{230}\text{Th}$ ratio influenced by particle composition

817 and remineralization, *Earth Planet. Sci. Lett.*, 167(3–4), 183–195,
818 doi:10.1016/S0012-821X(99)00035-7, 1999.
819 Luo, S. D., Ku, T. L., Kusakabe, M., Bishop, J. K. B. and Yang, Y. L.: Tracing particle
820 cycling in the upper ocean with Th-230 and Th-228: An investigation in the
821 equatorial Pacific along 140 degrees W, *Deep - Sea Res. Part II - Top. Stud. Oceanogr.*,
822 42(2–3), 805–829, doi:10.1016/0967-0645(95)00019-M, 1995.
823 Luo, Y., Francois, R. and Allen, S.: Sediment $^{231}\text{Pa}/^{230}\text{Th}$ as a recorder of the rate of
824 the Atlantic meridional overturning circulation: insights from a 2-D model, *Ocean*
825 *Sci.*, 6(3), 381–400, doi:10.5194/os-6-381-2010, 2010.
826 Mangini, A. and Diester-Hass, L.: Excess Th-230 in sediments off NW Africa traces
827 upwelling during the past 130,000 years, in *Coastal upwelling: Its sedimentary*
828 *records*, edited by E. Suess and J. Thiede, pp. 455–470, Plenum, 1983.
829 Mangini, A. and Key, R. M.: A ^{230}Th profile in the Atlantic Ocean, *Earth Planet. Sci.*
830 *Lett.*, 62(3), 377–384, doi:10.1016/0012-821X(83)90008-0, 1983.
831 Mangini, A. and Sonntag, C.: ^{231}Pa dating of deep-sea cores via ^{227}Th counting,
832 *Earth Planet. Sci. Lett.*, 37(2), 251–256, 1977.
833 Mangini, A. and U., K.: Depositional history in the Clarion-Clipperton zone during the
834 last 250,000 years: ^{230}Th and ^{231}Pa methods, *Geol. Jahrb.*, 87, 105–121, 1987.
835 Marchal, O., François, R., Stocker, T. F. and Joos, F.: Ocean thermohaline circulation
836 and sedimentary $^{231}\text{Pa}/^{230}\text{Th}$ ratio, *Paleoceanography*, 15(6), 625–641 [online]
837 Available from: <http://onlinelibrary.wiley.com/doi/10.1029/2000PA000496/full>
838 (Accessed 19 April 2016), 2000.
839 McManus, J., Francois, R. and Gherardi, J.: Collapse and rapid resumption of Atlantic
840 meridional circulation linked to deglacial climate changes, *Nature*, 428(6985), 834–
841 837, 2004.
842 Moore, J. K. and Braucher, O.: Sedimentary and mineral dust sources of dissolved
843 iron to the World Ocean, *Biogeosciences*, 5(1994), 631–656, doi:10.5194/bgd-4-
844 1279-2007, 2008.
845 Moore, J. K., Doney, S. C., Glover, D. M. and Fung, I. Y.: Iron cycling and nutrient-
846 limitation patterns in surface waters of the World Ocean, , 49, 463–507, 2002.
847 Moore, J. K., Doney, S. C. and Lindsay, K.: Upper ocean ecosystem dynamics and iron
848 cycling in a global three-dimensional model, *Global Biogeochem. Cycles*, 18(4),
849 doi:10.1029/2004GB002220, 2004.
850 Moore, J. K., Lindsay, K., Doney, S. C., Long, M. C. and Misumi, K.: Marine Ecosystem
851 Dynamics and Biogeochemical Cycling in the Community Earth System Model
852 [CESM1(BGC)]: Comparison of the 1990s with the 2090s under the RCP4.5 and
853 RCP8.5 Scenarios, *J. Clim.*, 26(23), 9291–9312, doi:10.1175/JCLI-D-12-00566.1,
854 2013.
855 Moore, R. M. and Hunter, K. A.: Thorium adsorption in the ocean: reversibility and
856 distribution amongst particle sizes, *Geochim. Cosmochim. Acta*, 49(11), 2253–2257,
857 doi:10.1016/0016-7037(85)90225-X, 1985.
858 Moore, W. S.: The thorium isotope content of ocean water, *Earth Planet. Sci. Lett.*,
859 53(3), 419–426, doi:10.1016/0012-821X(81)90046-7, 1981.
860 Moran, S. B., Hoff, J. A., Buesseler, K. O. and Edwards, R. L.: High precision ^{230}Th and
861 ^{232}Th in the Norwegian Sea and Denmark by thermal ionization mass
862 spectrometry, , 22(19), 2589–2592, 1995.

863 Moran, S. B., Charette, M. a., Hoff, J. a., Edwards, R. L. and Landing, W. M.: Distribution
864 of ^{230}Th in the Labrador Sea and its relation to ventilation, *Earth Planet. Sci. Lett.*,
865 150, 151–160, doi:10.1016/S0012-821X(97)00081-2, 1997.
866 Moran, S. B., Shen, C.-C., Weinstein, S. E., Hettlinger, L. H., Hoff, J. H., Edmonds, H. N.
867 and Edwards, R. L.: Constraints on deep water age and particle flux in the Equatorial
868 and South Atlantic Ocean based on seawater ^{231}Pa and ^{230}Th data, *Geophys. Res.*
869 *Lett.*, 28(18), 3437–3440 [online] Available from:
870 papers2://publication/uuid/2A811583-B32B-4BD8-B582-EC8B0D96A949, 2001.
871 Moran, S. B., Shen, C. C., Edmonds, H. N., Weinstein, S. E., Smith, J. N. and Edwards, R.
872 L.: Dissolved and particulate ^{231}Pa and ^{230}Th in the Atlantic Ocean: Constraints on
873 intermediate/deep water age, boundary scavenging, and $^{231}\text{Pa}/^{230}\text{Th}$
874 fractionation, *Earth Planet. Sci. Lett.*, 203(3–4), 999–1014, doi:10.1016/S0012-
875 821X(02)00928-7, 2002.
876 Müller, P. J. and Mangini, A.: Organic carbon decomposition rates in sediments of the
877 pacific manganese nodule belt dated by ^{230}Th and ^{231}Pa , *Earth Planet. Sci. Lett.*,
878 51(1), 94–114, doi:10.1016/0012-821X(80)90259-9, 1980.
879 Negre, C., Zahn, R., Thomas, A. L., Masqué, P., Henderson, G. M., Martínez-Méndez, G.,
880 Hall, I. R. and Mas, J. L.: Reversed flow of Atlantic deep water during the Last Glacial
881 Maximum., *Nature*, 468(7320), 84–88, doi:10.1038/nature09508, 2010.
882 Nozaki, Y. and Horibe, Y.: Alpha-emitting thorium isotopes in northwest Pacific deep
883 waters, *Earth Planet. Sci. Lett.*, 65(1), 39–50, doi:10.1016/0012-821X(83)90188-7,
884 1983.
885 Nozaki, Y. and Nakanishi, T.: ^{231}Pa and ^{230}Th profiles in the open ocean water
886 column, *Deep Sea Res. Part A, Oceanogr. Res. Pap.*, 32(10), 1209–1220,
887 doi:10.1016/0198-0149(85)90004-4, 1985.
888 Nozaki, Y. and Yamada, M.: Thorium and protactinium isotope distributions in
889 waters of the Japan Sea, *Deep Sea Res. Part A, Oceanogr. Res. Pap.*, 34(8), 1417–1430,
890 1987.
891 Nozaki, Y. and Yang, H. S.: Th and Pa isotopes in the waters of the western margin of
892 the pacific near Japan: Evidence for release of ^{228}Ra and ^{227}Ac from slope
893 sediments, *J. Oceanogr. Soc. Japan*, 43(4), 217–227, doi:10.1007/BF02109817, 1987.
894 Nozaki, Y., Horibe, Y. and Tsubota, H.: The water column distribution of thorium
895 isotopes in the western North Pacific, *Earth Planet. Sci. Lett.*, 54(54), 203–216, 1981.
896 Nozaki, Y., Yang, H.-S. and Yamada, M.: Scavenging of thorium in the ocean, *J.*
897 *Geophys. Res.*, 92(C1), 772, doi:10.1029/JC092iC01p00772, 1987.
898 Okubo, A., Obata, H., Nozaki, Y., Yamamoto, Y. and Minami, H.: ^{230}Th in the
899 Andaman Sea: Rapid deep-sea renewal, *Geophys. Res. Lett.*, 31(22), 1–5,
900 doi:10.1029/2004GL020226, 2004.
901 Okubo, A., Obata, H., Luo, S., Gamo, T., Yamamoto, Y., Minami, H. and Yamada, M.:
902 Particle flux in the twilight zone of the eastern Indian Ocean: A constraint from
903 ^{234}U - ^{230}Th and ^{228}Ra - ^{228}Th disequilibria, *Deep. Res. Part I Oceanogr. Res. Pap.*,
904 54(10), 1758–1772, doi:10.1016/j.dsr.2007.06.009, 2007a.
905 Okubo, A., Obata, H., Gamo, T., Minami, H. and Yamada, M.: Scavenging of ^{230}Th in
906 the Sulu Sea, *Deep. Res. Part II Top. Stud. Oceanogr.*, 54(1–2), 50–59,
907 doi:10.1016/j.dsr2.2006.02.016, 2007b.
908 Okubo, A., Obata, H., Gamo, T. and Yamada, M.: ^{230}Th and ^{232}Th distributions in

909 mid-latitudes of the North Pacific Ocean: Effect of bottom scavenging, *Earth Planet.*
910 *Sci. Lett.*, 339–340, 139–150, doi:10.1016/j.epsl.2012.05.012, 2012.

911 Rempfer, J., Stocker, T. F., Joos, F., Lippold, J. and Jaccard, S. L.: New insights into
912 cycling of ²³¹Pa and ²³⁰Th in the Atlantic Ocean, *Earth Planet. Sci. Lett.*, 468, 27–
913 37, doi:10.1016/j.epsl.2017.03.027, 2017.

914 Roberts, N. L., McManus, J. F., Piotrowski, A. M. and McCave, I. N.: Advection and
915 scavenging controls of Pa/Th in the northern NE Atlantic, *Paleoceanography*, 29(6),
916 668–679, doi:10.1002/2014PA002633, 2014.

917 Robinson, L. F., Belshaw, N. S. and Henderson, G. M.: U and Th concentrations and
918 isotope ratios in modern carbonates and waters from the Bahamas, *Geochim.*
919 *Cosmochim. Acta*, 68(8), 1777–1789, doi:10.1016/j.gca.2003.10.005, 2004.

920 Roy-Barman, M., Chen, J. H. and Wasserburg, G. J.: ²³⁰Th-²³²Th systematics in the
921 central Pacific Ocean: The sources and the fates of thorium, *Earth Planet. Sci. Lett.*,
922 139(3–4), 351–363, doi:10.1016/0012-821X(96)00017-9, 1996.

923 Rutgers van der Loeff, M. M. and Berger, G. W.: Scavenging of ²³⁰Th and ²³¹Pa near
924 the antarctic polar front in the South Atlantic, *Deep. Res. Part I*, 40(2), 339–357,
925 doi:10.1016/0967-0637(93)90007-P, 1993.

926 Schmittner, A.: Decline of the marine ecosystem caused by a reduction in the
927 Atlantic overturning circulation., *Nature*, 434(7033), 628–633,
928 doi:10.1038/nature03476, 2005.

929 Schmitz, W., Mangini, A., Stoffers, P., Glasby, G. P. and Pluger, W. L.: Sediment
930 accumulation rates in the southwestern Pacific Basin and Aitutaki Passage, *Mar.*
931 *Geol.*, 73(1), 181–190, 1986.

932 Scholten, J. C., Rutgers van der Loeff, M. M. and Michel, A.: Distribution of ²³⁰Th and
933 ²³¹Pa in the water column in relation to the ventilation of the deep Arctic basins,
934 *Deep. Res. Part II*, 42(6), 1519–1531, doi:10.1016/0967-0645(95)00052-6, 1995.

935 Scholten, J. C., Fietzke, J., Mangini, A., Stoffers, P., Rixen, T., Gaye-Haake, B., Blanz, T.,
936 Ramaswamy, V., Sirocko, F., Schulz, H. and Ittekkot, V.: Radionuclide fluxes in the
937 Arabian Sea: The role of particle composition, *Earth Planet. Sci. Lett.*, 230(3–4), 319–
938 337, doi:10.1016/j.epsl.2004.11.003, 2005.

939 Scholten, J. C., Fietzke, J., Mangini, A., Garbe-Schönberg, C. D., Eisenhauer, A.,
940 Schneider, R. and Stoffers, P.: Advection and scavenging: Effects on ²³⁰Th and
941 ²³¹Pa distribution off Southwest Africa, *Earth Planet. Sci. Lett.*, 271(1–4), 159–169,
942 doi:10.1016/j.epsl.2008.03.060, 2008.

943 Shimmield, G. B. and Price, N. B.: The scavenging of U,²³⁰Th and ²³¹Pa during
944 pulsed hydrothermal activity at 20°S, East Pacific Rise, *Geochim. Cosmochim. Acta*,
945 52(3), 669–677, doi:10.1016/0016-7037(88)90329-8, 1988.

946 Shimmield, G. B., Murray, J. W., Thomson, J., Bacon, M. P., Anderson, R. F. and Price, N.
947 B.: The distribution and behaviour of ²³⁰Th and ²³¹Pa at an ocean margin, Baja
948 California, Mexico, *Geochim. Cosmochim. Acta*, 50(11), 2499–2507,
949 doi:10.1016/0016-7037(86)90032-3, 1986.

950 Siddall, M., Henderson, G. M., Edwards, N. R., Frank, M., Müller, S. a., Stocker, T. F. and
951 Joos, F.: ²³¹Pa/²³⁰Th fractionation by ocean transport, biogenic particle flux and
952 particle type, *Earth Planet. Sci. Lett.*, 237(1–2), 135–155,
953 doi:10.1016/j.epsl.2005.05.031, 2005.

954 Siddall, M., Stocker, T. F., Henderson, G. M., Joos, F., Frank, M., Edwards, N. R., Ritz, S.

955 P. and Müller, S. a.: Modeling the relationship between $^{231}\text{Pa}/^{230}\text{Th}$ distribution
956 in North Atlantic sediment and Atlantic meridional overturning circulation,
957 *Paleoceanography*, 22(2), n/a-n/a, doi:10.1029/2006PA001358, 2007.
958 Thomas, A. L., Henderson, G. M. and Robinson, L. F.: Interpretation of the
959 $^{231}\text{Pa}/^{230}\text{Th}$ paleocirculation proxy: New water-column measurements from the
960 southwest Indian Ocean, *Earth Planet. Sci. Lett.*, 241(3-4), 493-504,
961 doi:10.1016/j.epsl.2005.11.031, 2006.
962 Trimble, S. M., Baskaran, M. and Porcelli, D.: Scavenging of thorium isotopes in the
963 Canada Basin of the Arctic Ocean, *Earth Planet. Sci. Lett.*, 222(3-4), 915-932,
964 doi:10.1016/j.epsl.2004.03.027, 2004.
965 Venchiarutti, C., van der Loeff, M. R. and Stimac, I.: Scavenging of ^{231}Pa and thorium
966 isotopes based on dissolved and size-fractionated particulate distributions at Drake
967 Passage (ANTXXIV-3), *Deep. Res. Part II Top. Stud. Oceanogr.*, 58(25-26), 2767-
968 2784, doi:10.1016/j.dsr.2.2010.10.040, 2011.
969 Vogler, S., Scholten, J., Rutgers van der Loeff, M. M. and Mangini, A.: ^{230}Th in the
970 eastern North Atlantic: the importance of water mass ventilation in the balance of
971 ^{230}Th , *Earth Planet. Sci. Lett.*, 156(1-2), 61-74, doi:10.1016/S0012-
972 821X(98)00011-9, 1998.
973 Walter, H. J., Rutgers van der Loeff, M. M. and Hoeltzen, H.: Enhanced scavenging of
974 ^{231}Pa relative to ^{230}Th in the South Atlantic south of the Polar Front: Implications
975 for the use of the $^{231}\text{Pa}/^{230}\text{Th}$ ratio as a paleoproductivity proxy, *Earth Planet. Sci.*
976 *Lett.*, 149(1), 85-100, doi:10.1016/S0012-821X(97)00068-X, 1997.
977 Yang, H. S., Nozaki, Y., Sakai, H. and Masuda, A.: The distribution of ^{230}Th and ^{231}Pa
978 in the deep-sea surface sediments of the Pacific Ocean, *Geochim. Cosmochim. Acta*,
979 50(1), 81-89, doi:10.1016/0016-7037(86)90050-5, 1986.
980 Yong-Liang Yang, Elderfield, H., Pedersen, T. F. and Ivanovich, M.: Geochemical
981 record of the Panama Basin during the Last Glacial Maximum carbon event shows
982 that the glacial ocean was not suboxic, *Geology*, 23(12), 1115-1118,
983 doi:10.1130/0091-7613(1995)023<1115:GROTPB>2.3.CO, 1995.
984 Yong Lao, Anderson, R. F., Broecker, W. S., Trumbore, S. E., Hofmann, H. J. and Wolfli,
985 W.: Transport and burial rates of ^{10}Be and ^{231}Pa in the Pacific Ocean during the
986 Holocene period, *Earth Planet. Sci. Lett.*, 113(1-2), 173-189, doi:10.1016/0012-
987 821X(92)90218-K, 1992.
988 Yu, E.-F.: Variations in the Particulate Flux of ^{230}Th and ^{231}Pa and
989 Paleoceanographic Applications of the $^{231}\text{Pa}/^{230}\text{Th}$ Ratio, WHOI/MIT., 1994.
990 Yu, E.-F., Francois, R. and Bacon, M. P.: Similar rates of modern and last-glacial ocean
991 thermohaline circulation inferred from radiochemical data, *Nature*, 379(6567),
992 689-694, doi:10.1038/379689a0, 1996.
993

Variable	Symbol	Value	Units
Production of ^{231}Pa from U decay	β^{Pa}	$2.33 \cdot 10^{-3}$	$\text{dpm m}^{-3} \text{ yr}^{-1}$
Production of ^{230}Th from U decay	β^{Th}	$2.52 \cdot 10^{-2}$	$\text{dpm m}^{-3} \text{ yr}^{-1}$
Decay constant of ^{231}Pa	λ^{Pa}	$2.13 \cdot 10^{-5}$	yr^{-1}
Decay constant of ^{230}Th	λ^{Th}	$9.22 \cdot 10^{-6}$	yr^{-1}
Index for ^{231}Pa and ^{230}Th	i		
Index for particle type	j		
Total isotope activity	A_t		dpm m^{-3}
Dissolved isotope activity	A_d		dpm m^{-3}
Particle associated activity	A_p		dpm m^{-3}
Particle settling velocity	w_s	1000	m yr^{-1}
Particle concentration	C		kg m^{-3}
Density of seawater		1024.5	kg m^{-3}
Ratio between particle concentration and density of seawater	R		

994 Table 1. List of parameters, abbreviations and values.

995

996

	CTRL		EXP_1		EXP_2	
	^{231}Pa	^{230}Th	^{231}Pa	^{230}Th	^{231}Pa	^{230}Th
K_{CaCO_3}	$2.5 \cdot 10^5$	$1.0 \cdot 10^7$	$5 \cdot 10^4$	$2 \cdot 10^6$	$1.25 \cdot 10^6$	$5 \cdot 10^7$
K_{Opal}	$1.67 \cdot 10^6$	$5 \cdot 10^5$	$3.33 \cdot 10^5$	$1 \cdot 10^5$	$8.33 \cdot 10^6$	$2.5 \cdot 10^6$
K_{POC}	$1.0 \cdot 10^7$	$1.0 \cdot 10^7$	$2 \cdot 10^6$	$2 \cdot 10^6$	$5 \cdot 10^7$	$5 \cdot 10^7$
τ (yr)	118	33	501	143	27	9

997 Table 2. Partition coefficients for different particle types and residence time for

998 ^{231}Pa and ^{230}Th in different experiments. Partition coefficients used in CTRL follows

999 (Chase et al., 2002; Siddall et al., 2005). Both p-coupled and p-fixed versions are

1000 enabled in CTRL, which yields identical results (discussed in section 4.1). Only p-

1001 fixed version is enabled in Exp_1 and Exp_2. The residence time (τ) is for p-fixed

1002 version in each experiment.

1003

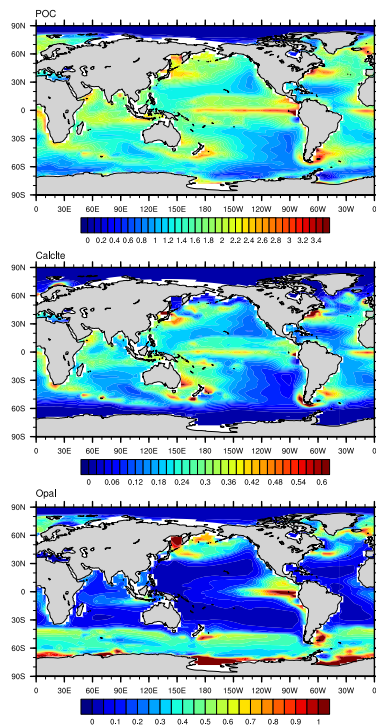
WATER COLUMN ACTIVITY	Holocene core-top $^{231}\text{Pa}/^{230}\text{Th}$
(Guo et al., 1995)	(Yu, 1994)
(Cochran et al., 1987)	(DeMaster, 1979)
(Nozaki et al., 1987)	(Bacon and Rosholt, 1982)
(Bacon and Anderson, 1982)	(Mangini and Diester-Hass, 1983)
(Bacon et al., 1989)	(Kumar, 1994)

(Huh and Beasley, 1987)	(Yang et al., 1986)
(Rutgers van der Loeff and Berger, 1993)	(Anderson et al., 1983)
(Nozaki et al., 1981)	(Anderson et al., 1994)
(Nozaki and Nakanishi, 1985)	(Ku, 1966)
(Mangini and Key, 1983)	(Ku et al., 1972)
(Nozaki and Horibe, 1983)	(Frank et al., 1994)
(Moore, 1981)	(Shimmield et al., 1986)
(Nozaki and Yamada, 1987)	(Frank, 1996)
(Roy-Barman et al., 1996)	(Yong Lao et al., 1992)
(Nozaki and Yang, 1987)	(Francois et al., 1993)
(Moran et al., 1995)	(Anderson et al., 1990)
(Luo et al., 1995)	(Mangini and Sonntag, 1977)
(Colley et al., 1995)	(Schmitz et al., 1986)
(Scholten et al., 1995)	(Shimmield and Price, 1988)
(Cochran et al., 1995)	(Yong-Liang Yang et al., 1995)
(Vogler et al., 1998)	(Müller and Mangini, 1980)
(Moran et al., 1997)	(Mangini and U., 1987)
(Edmonds et al., 1998)	(Scholten et al., 1995)
(Moran et al., 2001)	(Walter et al., 1997)
(Edmonds et al., 2004)	(Lippold et al., 2011)
(Okubo et al., 2007b)	(Lippold et al., 2012b)
(Coppola et al., 2006)	(Bradtmiller et al., 2007)
(Moran et al., 2002)	(Gherardi et al., 2005)
(Okubo et al., 2004)	(Gutjahr et al., 2008)
(Okubo et al., 2007a)	(Hall et al., 2006)
(Okubo et al., 2012)	(Lippold et al., 2011)
(Robinson et al., 2004)	(Roberts et al., 2014)
(Thomas et al., 2006)	(Bradtmiller et al., 2014)
(Trimble et al., 2004)	(Burckel et al., 2016)
(Venchiarutti et al., 2011)	(Hoffmann et al., 2013)
(Hsieh et al., 2011)	(Jonkers et al., 2015)
(Scholten et al., 2008)	(Negre et al., 2010)
(Luo et al., 2010)	
(Deng et al., 2014)	
(Hayes et al., 2013)	
(Hayes et al., 2015)	

1004
1005
1006
1007
1008
1009
1010

Table 3. References for observations of water column ^{231}Pa and ^{230}Th activity (left column) and Holocene core-top $^{231}\text{Pa}/^{230}\text{Th}$ (right column).

1011 Figures:

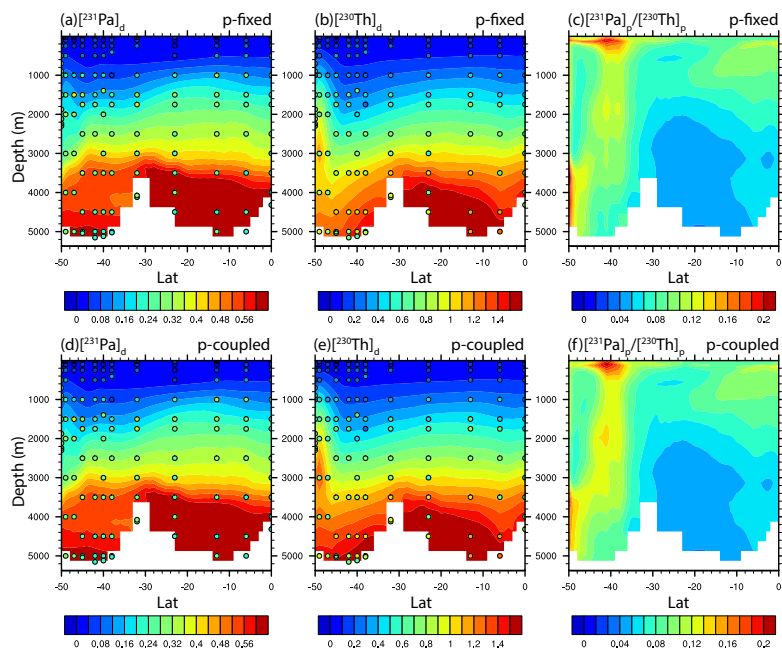


1012

1013 Figure 1. Annual mean particle fluxes in CESM. (a) CaCO_3 flux at 105m ($\text{mol m}^{-2} \text{yr}^{-1}$).

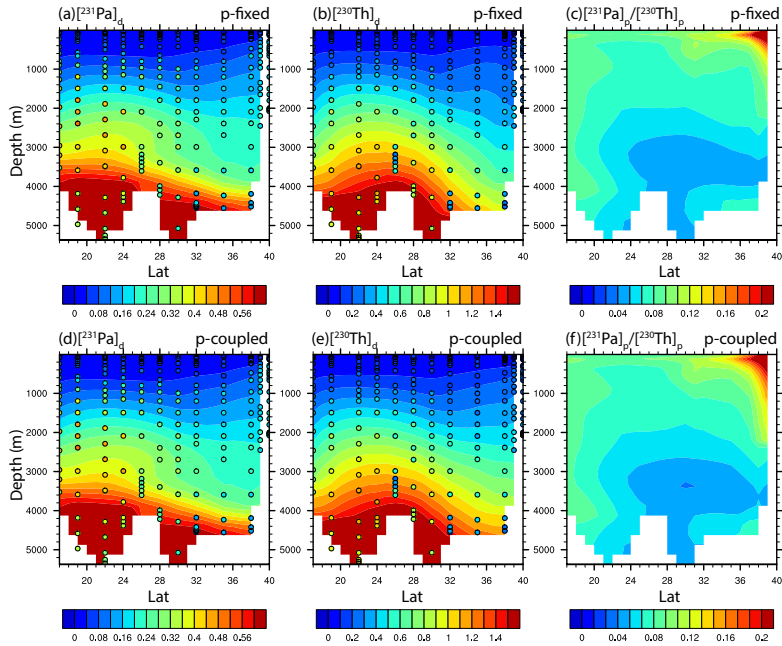
1014 (b) Opal flux at 105m ($\text{mol m}^{-2} \text{yr}^{-1}$). (c) POC flux at 105m ($\text{mol m}^{-2} \text{yr}^{-1}$).

1015

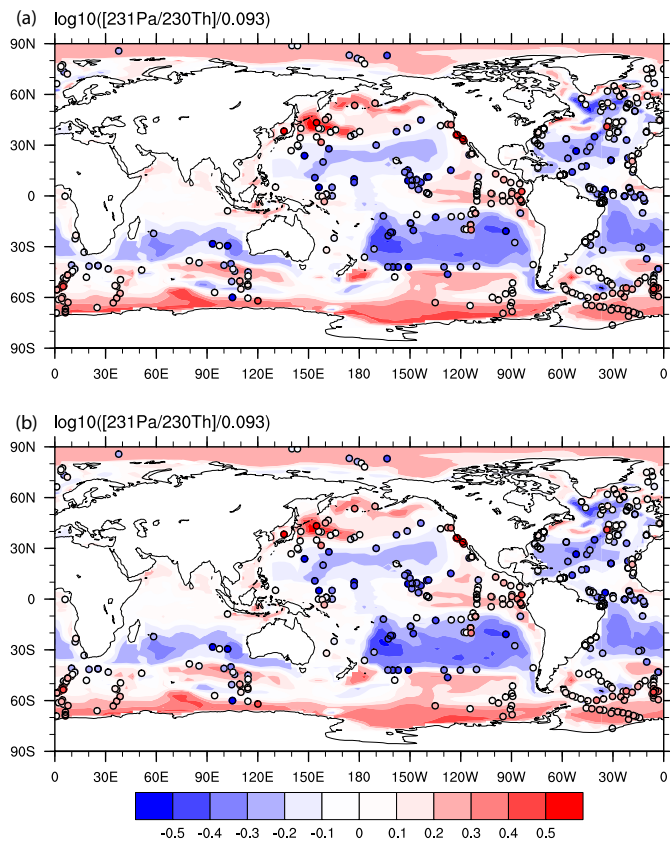


1017

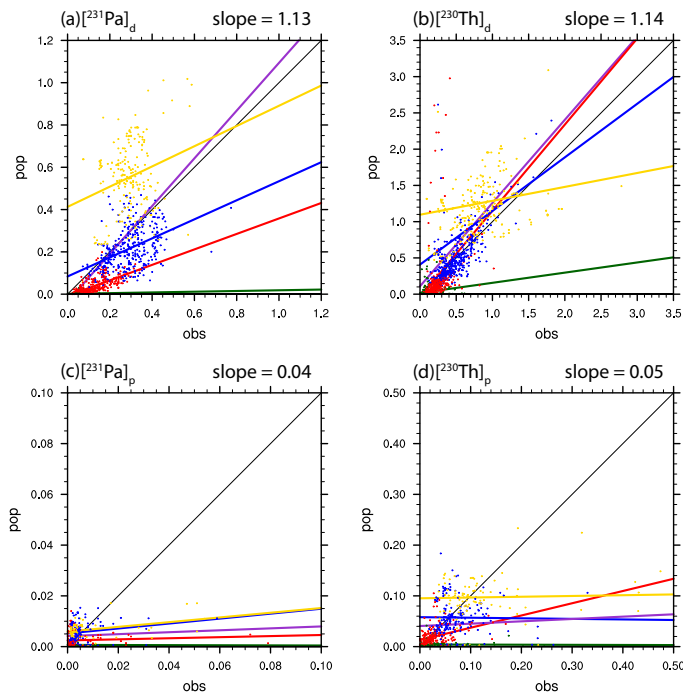
1018 Figure 2. Dissolved ^{231}Pa , dissolved ^{230}Th and particulate $^{231}\text{Pa}/^{230}\text{Th}$ in CTRL along
 1019 GEOTRACES transect GA02S (Deng et al., 2014) (the track is indicated in Fig. S4) for
 1020 both p-fixed (top row) and p-coupled (bottom row) ^{231}Pa and ^{230}Th (colored
 1021 contour). Observations of dissolved ^{231}Pa and ^{230}Th activity are superimposed as
 1022 colored circles using the same color scale.



1023
 1024 Figure 3. Dissolved ^{231}Pa , dissolved ^{230}Th and particulate $^{231}\text{Pa}/^{230}\text{Th}$ in CTRL along
 1025 GEOTRACES transect GA03 (Hayes et al., 2015) (the track is indicated in Fig. S4) for
 1026 both p-fixed (top row) and p-coupled (bottom row) ^{231}Pa and ^{230}Th (colored
 1027 contours). Observations of dissolved ^{231}Pa and ^{230}Th activity are superimposed as
 1028 colored circles using the same color scale.



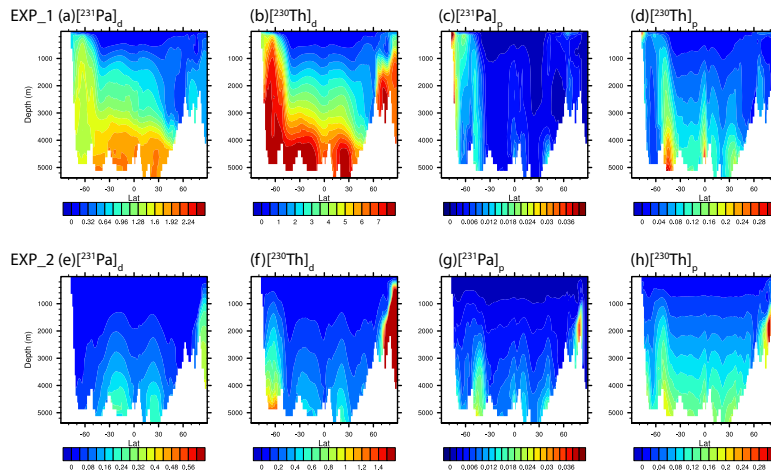
1029
 1030 Figure 4. Sediment $^{231}\text{Pa}/^{230}\text{Th}$ activity ratio in CTRL for both p-fixed (a) and p-
 1031 coupled version (b). Observations are attached as filled cycles using the same color map.
 1032 The $^{231}\text{Pa}/^{230}\text{Th}$ activity ratio is plotted relative to the production ratio of
 1033 0.093 on a \log_{10} scale.
 1034
 1035
 1036



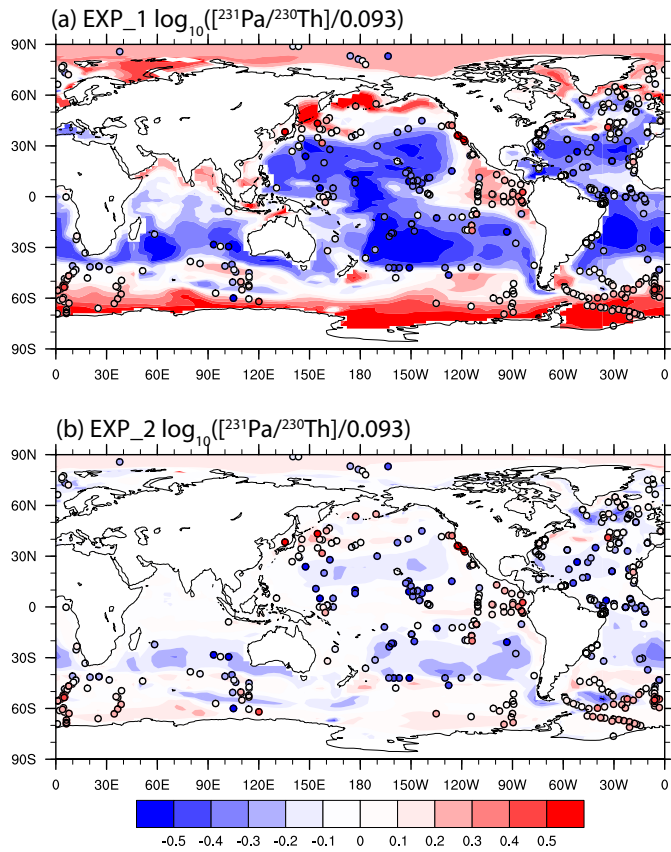
1037

1038

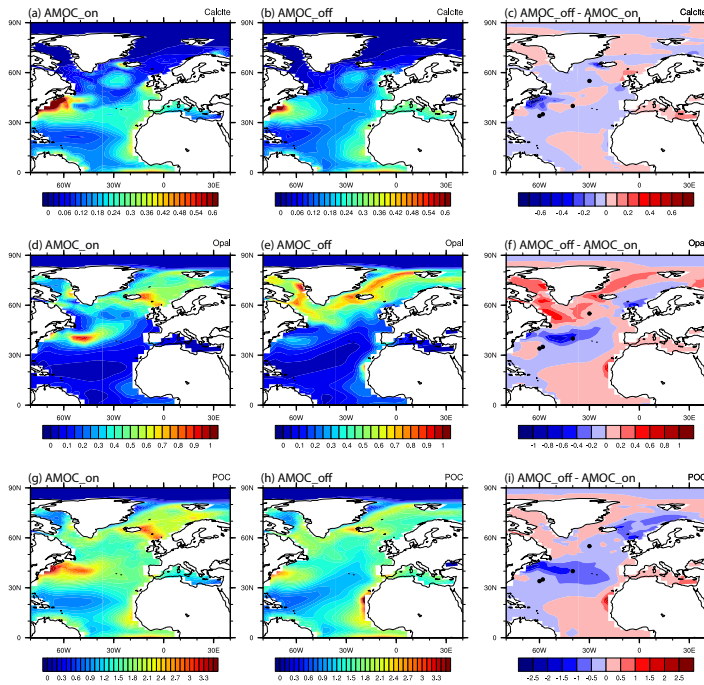
1039 Figure 5. Scatter plot of global dissolved and particulate ^{231}Pa and ^{230}Th between
 1040 observation and CTRL (p-fixed) (unit: dpm/m^3). (a) dissolved ^{231}Pa ; (b) particulate
 1041 ^{231}Pa ; (c) dissolved ^{230}Th ; (d) particulate ^{230}Th . Observations in different depth
 1042 range are indicated by different colors: green for 0-100m; red for 100m-1,000m;
 1043 blue for 1,000m-3,000m and yellow for deeper than 3,000m. Purple line is the least
 1044 squared linear regression line for all depth range, the slope of which is indicated at
 1045 the top right of each plot. Green line is the least squared linear regression line for
 1046 depth from 0-100m. Red line is the least squared linear regression line for depth
 1047 from 100m -1,000m. Blue line is the least squared linear regression line for depth
 1048 from 1,000m-3,000m. Yellow line is the least squared linear regression line for
 1049 depth deeper than 3,000m.



1050
 1051 Figure 6. Atlantic zonal mean dissolved and particulate ^{231}Pa and ^{230}Th in EXP_1 and
 1052 EXP_2 (unit: dpm/m^3). EXP_1: (a) dissolved ^{231}Pa ; (b) dissolved ^{230}Th ; (c)
 1053 particulate ^{231}Pa ; (d) particulate ^{230}Th . EXP_2: (e) dissolved ^{231}Pa ; (f) dissolved
 1054 ^{230}Th ; (g) particulate ^{231}Pa ; (h) particulate ^{230}Th .
 1055

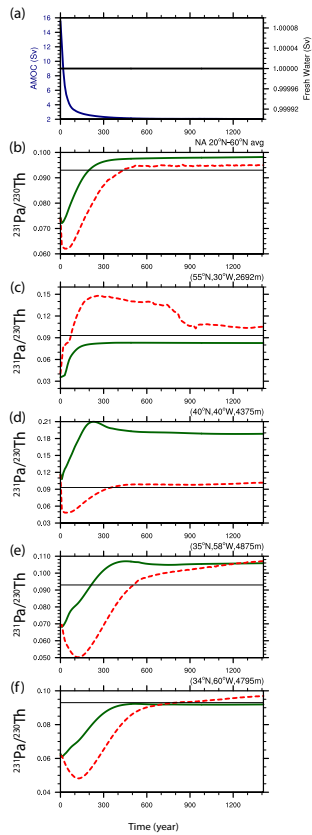


1056
 1057 Figure 7. Sediment $^{231}\text{Pa}/^{230}\text{Th}$ activity ratio in EXP_1 (a) and EXP_2 (b).
 1058 Observations are attached as filled cycles using the same color map. The $^{231}\text{Pa}/^{230}\text{Th}$
 1059 activity ratio is plotted relative to the production ratio of 0.093 on a \log_{10} scale.
 1060



1061
 1062 Figure 8. Comparison of particle fluxes between AMOC_on and AMOC_off. CaCO₃ flux
 1063 at 105m (mol m⁻² yr⁻¹) during AMOC_on (a), AMOC_off (b) and difference between
 1064 AMOC_off and AMOC_on. (b) Opal flux at 105m (mol m⁻² yr⁻¹) during AMOC_on (d),
 1065 AMOC_off (e) and difference between AMOC_off and AMOC_on (f). POC flux at 105m
 1066 (mol m⁻² yr⁻¹) during AMOC_on (g), AMOC_off (h) and difference between AMOC_off
 1067 and AMOC_on (i).

1068
 1069

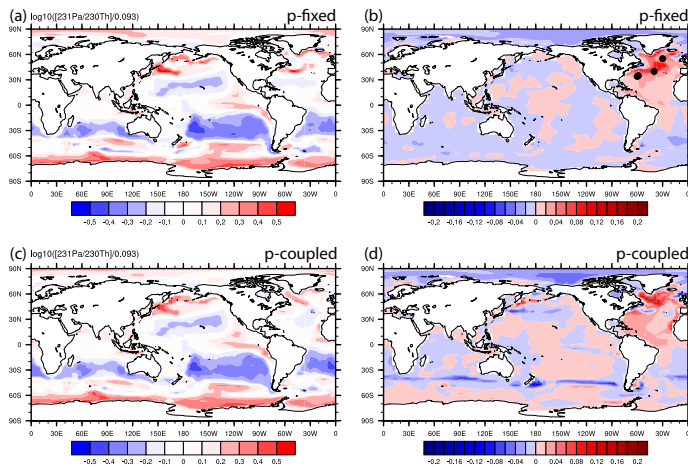


1070

1071

1072 Figure 9. Time evolutions in HOSING. (a) Freshwater forcing (black) and AMOC
 1073 strength (navy), which is defined as the maximum of the overturning
 1074 streamfunction below 500m in the North Atlantic. (b) North Atlantic average
 1075 sediment $^{231}\text{Pa}/^{230}\text{Th}$ activity ratio from 20°N to 60°N: p-fixed (green) and p-
 1076 coupled (red). Production ratio of 0.093 is indicated by a solid black line (similar in
 1077 c, d, e and f). (c) Sediment $^{231}\text{Pa}/^{230}\text{Th}$ activity ratio at (55°N, 30°W). (d) Sediment
 1078 $^{231}\text{Pa}/^{230}\text{Th}$ activity ratio at (40°N, 40°W). (e) Sediment $^{231}\text{Pa}/^{230}\text{Th}$ activity ratio at
 1079 (35°N, 58°W). (f) Sediment $^{231}\text{Pa}/^{230}\text{Th}$ activity ratio at (34°N, 60°W). (e) and (f) are
 1080 near Bermuda Rise. Locations of each site are shown as dots in Fig. 8b.

1081

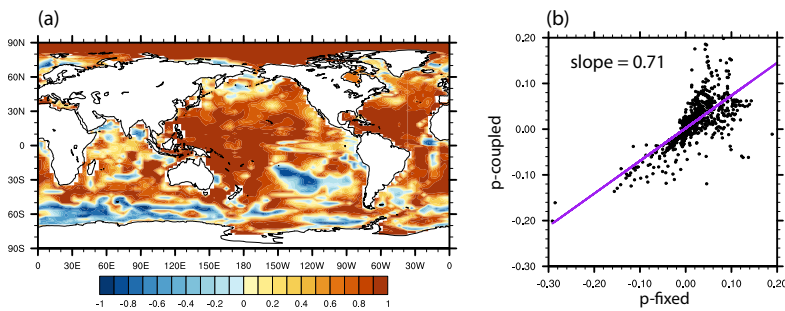


1082

1083

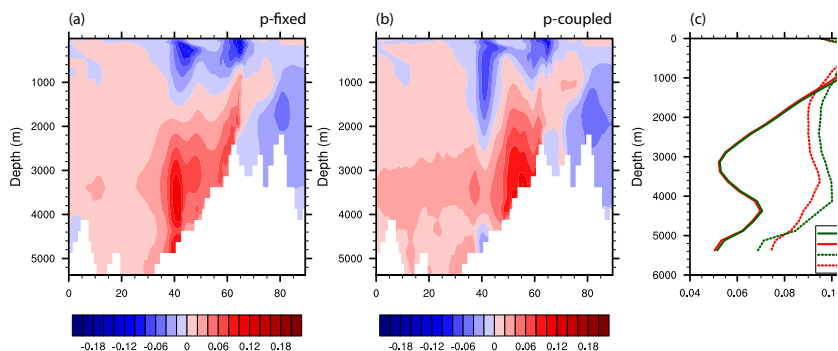
1084 Figure 10. Sediment $^{231}\text{Pa}/^{230}\text{Th}$ activity ratio during AMOC off state and the
1085 difference between AMOC off and CTRL. (a) P-fixed $\log_{10}([^{231}\text{Pa}/^{230}\text{Th}]/0.093)$ in
1086 AMOC_off. (b) Difference of p-fixed sediment $^{231}\text{Pa}/^{230}\text{Th}$ activity ratio between
1087 AMOC_off and AMOC_on. (c) and (d) are similar to (a) and (b) for p-coupled
1088 sediment $^{231}\text{Pa}/^{230}\text{Th}$ activity ratio. Black dots in (b) shows the locations of sites in
1089 Fig. 9 from North to South.

1090



1091

1092 Figure 11. (a) Correlation of p-fixed and p-coupled evolution of sediment
1093 $^{231}\text{Pa}/^{230}\text{Th}$ activity ratio in HOSING. (b) Scatter plot of p-fixed and p-coupled
1094 sediment $^{231}\text{Pa}/^{230}\text{Th}$ activity ratio change from AMOC_on to AMOC_off in the
1095 Atlantic and the Southern Ocean (70°W-20°E). Purple line is the least squared linear
1096 regression line and slope is the linear regression coefficient.
1097



1098
1099 Figure 12. Difference of Atlantic zonal mean particulate $^{231}\text{Pa}/^{230}\text{Th}$ between
1100 AMOC_off and AMOC_on: (a) p-fixed and (b) p-coupled. (c) North Atlantic (20°N-
1101 60°N) average profile during AMOC_on (solid) and AMOC_off (dash) for p-fixed
1102 (green) and p-coupled (red) particulate $^{231}\text{Pa}/^{230}\text{Th}$.
1103
1104
1105
1106